Evaluation of cloud microphysics simulated using a meso-scale model coupled with a spectral bin microphysical scheme through comparison with observation data by ship-borne Doppler and space-borne W-band radars

T. Iguchi, T. Nakajima, A. P. Khain, K. Saito, T. Takemura, H. Okamoto,
T. Nishizawa, and W.-K. Tao

Submitted to J. Geophy. Res.

Equivalent radar reflectivity factors (Ze) measured by W-band radars are directly compared with the corresponding values calculated from a three-dimensional non-hydrostatic meso-scale model coupled with a spectral-bin-microphysical (SBM) scheme for cloud. Three case studies are the objects of this research: one targets a part of ship-borne observation using 95 GHz Doppler radar over the Pacific Ocean near Japan in May 2001; other two are aimed at two short segments of space-borne observation by the cloud profiling radar on CloudSat in November 2006. The numerical weather prediction (NWP) simulations reproduce general features of vertical structures of Ze and Doppler velocity. A main problem in the reproducibility is an overestimation of Ze in ice cloud layers. A frequency analysis shows a strong correlation between ice water contents (IWC) and Ze in the simulation; this characteristic is similar to those shown in prior on-site studies.

From comparing with the empirical correlations by the prior studies, the simulated Ze is overestimated than the corresponding values in the studies at the same IWC. Whereas the comparison of Doppler velocities suggests that large-size snowflakes are necessary for producing large velocities under the freezing level and hence rules out the possibility that an overestimation of snow size causes the overestimation of Ze. Based on the results of several sensitivity tests, we conclude that the source of the overestimation is a bias in the microphysical calculation of Ze or an overestimation of IWC. To identify the source of the problems needs further validation research with other follow-up observations.

Evaluation of cloud microphysics simulated using a meso-scale model coupled with a spectral bin microphysical scheme through comparison with observation data by ship-borne Doppler and space-borne W-band radars.

T. Iguchi
Earth System Science Interdisciplinary Center, University of Maryland, College Park, Maryland, USA

T. Nakajima
Center for Climate System Research, The University of Tokyo, Kashiwa, Japan

A. P. Khain
Department of Atmospheric Sciences, Institute of the Earth Science, The Hebrew University of Jerusalem, Jerusalem, Israel

K. Saito
Meteorological Research Institute, Tsukuba, Japan

T. Takemura
Research Institute for Applied Mechanics, Kyushu University, Fukuoka, Japan

H. Okamoto
Graduate School of Science, Tohoku University, Sendai, Japan

T. Nishizawa
National Institute for Environmental Studies, Tsukuba, Japan

W.-K. Tao
Laboratory for Atmospheres, NASA Goddard Space Flight Center, Greenbelt, Maryland, USA

Submitted to *J. Geophys. Res.*

Corresponding author
Takamichi Iguchi
Code 613.1

NASA- Goddard Space Flight Center
(301)614-6225
Takamichi.Iguchi@nasa.gov

Abstract

Equivalent radar reflectivity factors (Ze) measured by W-band radars are directly compared with the corresponding values calculated from a three-dimensional non-hydrostatic meso-scale model coupled with a spectral-bin-microphysical (SBM) scheme for cloud. Three case studies are the objects of this research: one targets a part of ship-borne observation using 95 GHz Doppler radar over the Pacific Ocean near Japan in May 2001; other two are aimed at two short segments of space-borne observation by the cloud profiling radar on CloudSat in November 2006. The numerical weather prediction (NWP) simulations reproduce general features of vertical structures of Ze and Doppler velocity. A main problem in the reproducibility is an overestimation of Ze in ice cloud layers. A frequency analysis shows a strong correlation between ice water contents (IWC) and Ze in the simulation; this characteristic is similar to those shown in prior on-site studies. From comparing with the empirical correlations by the prior studies, the simulated Ze is overestimated than the corresponding values in the studies at the same IWC. Whereas the comparison of Doppler velocities suggests that large-size snowflakes are necessary for producing large velocities under the freezing level and hence rules out the possibility that an overestimation of snow size causes the overestimation of Ze. Based on the results of several sensitivity tests, we conclude that the source of the overestimation is a bias in the microphysical calculation of Ze or an overestimation of IWC. To identify the source of the problems needs further validation research with other follow-up observations.

1. Introduction

Remote-sensing using a radar/lidar is useful to observe a distribution and density of cloud and precipitation. W-band cloud radars for frequency ranging from 75 to 111 GHz can observe small particles of several micrometers such as cloud droplets with large Rayleigh scattering, which cannot be detected by C-band or X-band precipitation radars. A frequency around 94 GHz in W-band is popularly used to monitor cloud and precipitation due to a small attenuation by atmospheric gas absorption at the frequency [*Lhermitte*, 1987, Figure 1]. Many observations using ground-based, ship-borne, or air-borne W-band radars were reported by prior studies [e.g., *Clothiaux et al.*, 1995]. Furthermore, the CloudSat satellite with a 94 GHz Cloud Profiling Radar (CPR) was launched in April 2006 and then the data have been compiled [*Stephens et al.*, 2002; 2008]. Global observation by A-train satellites including CloudSat is providing significant information on structures of cloud and precipitation. Also the mission of EarthCARE satellite is currently in the preparation stage; both 94 GHz Doppler radar and lidar will be loaded on the satellite. Thus the present time is very appropriate for studies using datasets from such radars.

Validation of cloud modeling is a way to make use of measurements with cloud radars. Most prior studies used a radar-signal simulation package, e.g. QuickBeam [*Haynes et al.*, 2007], to calculate an equivalent radar reflectivity factor (Ze) from prognostic variables, which is corresponding to the actually measured Ze; this approach enabled a direct signal-based comparison. As an example of such studies, a global output of a Multiscale Modeling Framework (MMF) was compared with CloudSat CPR observation [*Marchand et al*., 2008]. Tropical cloud and precipitation in MJO simulation using a global cloud resolving model (GCRM) with the horizontal grid size of several kilometers were compared with data sets of CloudSat CPR and TRMM Precipitation Radar (PR) [*Miura et al*., 2007; *Masunaga et al*., 2008] and Cloud-Aerosol Lidar and Infrared Pathfinder Satellite Observation (CALIPSO)/CloudSat satellite remote-sensings [*Inoue et al*., 2009; *Satoh et al*., 2009]. Global distributions and densities of cloud and precipitation in the Met office global model were evaluated using Cloudsat CPR data [*Bodas-Salcedo et al*., 2008]. Vertical structures of mid-latitude cloud observed using ship-borne radar and lidar were compared with those simulated by CCSR-NIES Atmospheric General Circulation Model (AGCM) [*Okamoto et al*., 2007].

In this study, we conducted three case studies; results of numerical weather prediction (NWP) simulations were compared with the observations by ship-borne or space-borne W-band radars for specific mid-latitude samples. A spectral-bin-microphysical (SBM) scheme for cloud was employed in the meso-scale model. The corresponding variables in the measurement products such as Ze and Doppler velocity (DV) were calculated using a newly developed radar-signal simulator modulated for the SBM scheme. This approach merits the following significance: It is more reasonable to conduct the signal-based comparison for the bin model simulation, both than the similar comparison of the bulk model simulation and than the retrieval-based comparison on physical parameters using a radar-only observation. The radar-signal simulator modulated for the SBM model utilizes particle size distributions (PSD) of hydrometeors directly given from the simulation, although the prognostic PSDs may include some errors. In contrast, a simulator for the bulk model needs some assumptions of the built-in PSDs matched to the prognostic mixing ratios; the type and shape of the function has an impact on a radar signal computed through the simulator [e.g. *Bodas-Salcedo et al*., 2008, Figure 10]. Also a radar-only retrieval algorithm needs similar assumptions [e.g. *Austin et al*., 2008]; thus for example, their retrieved values of liquid water content (LWC) and ice water content (IWC) are dependent on the assumptions [e.g. *Woods et al*., 2008]. Note that quantitative evaluation of considering effects of nonsphericity and inhomogeneousity of ice particles is beyond the scope of this paper. Although they are further important problems in calculation or retrieval of a radar-signal, we expect that a detailed analysis of these effects is conducted in future research and then uncertainty associated with this point is expected to be reduced.

One case study is aimed at the part of observation by a 95 GHz Doppler radar on the research vessel during the cruise over the Pacific Ocean near Japan in May 2001. Other two case studies targets very short segments around Japan in November 2006 in CloudSat global observation using the 94GHz CPR. A composite view to the cases may produce a better analysis independent of a direction of passive remote sensing, although weather conditions and locations are different. These measurements have different in-between atmospheric components and instrument environments which can affect products of radar-signals and cause an uncertainty.

In this paper, the methodology is described in section 2, which includs the description of the NWP model and the explanation of the radar-signal simulator and radar observations. The results of numerical experiments and comparisons with the observations are shown in section 3. Summary and conclusions are finally given in section 4.

2. Methodology

2.1 Description of the meso-scale model for NWP simulation

The simulations were conducted using a three-dimensional non-hydrostatic meso-scale model coupled with a SBM scheme for cloud. The main framework is provided from the operational version of the Japan Meteorological Agency Nonhydrostatic model (JMA-NHM) [*Saito et al.*, 2006]. The basic governing equations are fully compressive nonhydrostatic equations. The time-splitting, horizontally explicit and vertically implicit (HE-VI) scheme is used to inhibit an inflation of sound waves. The Arakawa-C and Lorentz grid structures are employed in the horizontal and vertical grid discretizations, respectively. As for different points from the original, the broad band radiative transfer code “mstrn-x” [*Nakajima et al.*, 2000; *Sekiguchi and Nakajima*, 2008] is employed to calculate atmospheric radiation in the JMA-NHM simulations. The convective parameterization scheme in the operational version of JMA-NHM is not used to prevent a conflict with the under-mentioned SBM scheme.

The SBM microphysics scheme for cloud was implemented into the meso-scale model framework [*Iguchi et al.*, 2008], based on the module package of the Hebrew University Cloud Model (HUCM) [e.g., *Khain et al.*, 2000]. Hydrometeors are categorized into one-water and six-ice types: water droplets, ice crystals (plate, column, dendrite), snowflakes, graupel, and hail. The snowflakes, graupel, and hail are assumed to be spheres in the calculation of their microphysics [*Khain and Sednev*, 1995]. The discrete size distributions of hydrometeors are represented on a grid containing 33 doubling mass bins covering particles sizes in the range 2 mm < r < 3251 mm in terms of melted-particle radius. The scheme employs the equations to calculate the processes of nucleation for droplets and ice crystals, condensation and deposition growth, evaporation, sublimation, droplet freezing, melting, and coalescence growth [*Iguchi et al.*, 2008, Appendix A].

A bulk microphysics scheme is originally employed in the same model framework, and the result using it is suggested also. It is single-moment bulk scheme accounting for explicit two-water and three-ice types: cloud water, rain, cloud ice, snow, and graupel [*Lin et al.*, 1983; *Ikawa and Saito*, 1991; *Yamada*, 2003]. The Kessler's auto-conversion formula is employed to calculate the production rate of rain through accretion of cloud water by rain. The gravitational sedimentation of particles categorized as cloud water and cloud ice is assumed to be neglected due to the tiny terminal velocities.

2.2 Radar-signal products (Ze and Doppler velocity) simulator

The fundamental conception of the simulator is similar to those of, e.g. *Quickbeam* [*Haynes et al.*, 2007]. The simulator offline-converts prognostic variables from a model simulation to Ze and DV corresponding to the variables of radar measurement products. The attenuations due to atmospheric hydrometeors components and environment of the instrument were modeled in the simulator; hence, no attenuation correction is applied to radar-measured Ze. This approach enables a direct comparison with calibrated reflectivities from radar measurement.

The Mie solution was applied to estimate the scattering signatures of hydrometeors particles at frequencies of 94 and 95 GHz. Ze at a precipitation radar's frequency is often calculated on the basis of the Rayleigh scatter solution; the Ze is approximately proportional to the six powers of particles diameter in the Rayleigh regime. Whereas at 94 GHz, the transition from Rayleigh to Mie scatters occurs for the particles diameter about 0.8 mm [*Lhermitte*, 1987, Figure 9]. Thus the Ze of such larger particles does not follow the six power law at the frequency.

The equivalent radar reflectivity factor, Ze is given by [*Okamoto et al.*, 2003, Equation 13]

$$Z_e = \frac{\lambda^4}{\pi^5 |K|^2} \left[\int_{r_{\min}}^{r_{\max}} \frac{dn(r)}{dr} C_{bk}(r) dr \right], \quad (1)$$

where λ is the wavelength, r is the radius of particles, n is the size distributions of particles, and C_{bk} is the backscattering cross section as a function of radius and complex refractive indices. K is the dielectric factor estimated from m by $|K|=|(m^2-1)/(m^2+2)|$, m being complex refractive index. $|K|$ is set to be 0.828 for the MIRAI case and 0.75 for the CloudSat case. $|K|$ is assumed to be the same to both water and ice in this analysis; this assumption is based on the definition of Ze in each observation. The logarithmic form, $dBZe = 10\log_{10}Ze$, expressed in the unit of decibel (dB) is used.

Backscattering cross sections of ice particles (i.e. three-types ice crystals, snowflakes, graupel, and hail) are decided regardless of their effective or bulk densities. Mass equivalent volume with density of 0.9 g/cm^3 is defined for each mass bin and then the backscattering cross section is calculated on the sphere particle with the equivalent volume. This assumption is simple but adequate even as compared to a complex calculation considering a non-spherical and inhomogeneous particle. *Okamoto* [2002], and *Sato and Okamoto* [2006] suggested the intensive discrete dipole approximation (DDA) computations for hexagonal ice crystals with various shapes. The DDA computations with sufficient accuracy showed discrepancies in backscattering signatures for different shapes having the same volume were within about 2 dB as long as the volume equivalent radius was less than 200 micro meters.

In the case of applying the SBM model, prognostic PSDs of hydrometeors are directly substituted for the Eq. (1). The backscattering cross section, C_{bk} is given from the lookup table of the scattering properties pre-calculated on the basis of the Mie solution. Whereas in a case of applying the bulk model, prognostic mixing ratios of hydrometers are expanded to a size distribution spectrum on the same size bins using built-in PSDs. Generalized gamma distributions was assumed to be the built-in functions (BIFs), and their coefficients were referred to those in *Seifert and Beheng* [2006, Table1]. The mean particle radii are assumed to be approximately 10, 203, 10, 99, and 109 micro meters for the types of cloud water, rain, cloud ice, snow, and graupel, respectively. Then the calculation is processed the same as in the SBM model case.

The attenuated Ze by atmospheric components is given by

$$Z_{e,A} = Z_e \exp(-2\tau), \quad (2)$$

where τ is the optical thickness at the radar wavelength from the radar to the targeted layer, which is the integral of extinction coefficient. The actual integrations start from the surface in a ship-borne observation case and from the height of 705 km in a space-borne observation case. Extinction of hydrometeors particles were considered, whereas gas absorption such as vapor was assumed to be negligible in this study for a mid-latitude region. The extinction coefficients of hydrometeors are given from the pre-calculated lookup table for the mass bins. Only in the case of ship-borne radar on the MIRAI, the radar signal is attenuated by water originated in precipitation stagnant on the redome, which is a shield covering the radar container. This attenuation effect was introduced on the basis of *Okamoto et al*. [2007]; 9 dB was subtracted uniformly in the all vertical layers when the precipitation rate on the model surface grid is more than 0.5 mm/hour.

Doppler velocity v_d is defined as the sum of reflectivity-weighted particle fall velocity and vertical wind velocity, given in the modified form of *Matrosov et al*. [1994, Equations 1 and 7]:

$$v_d = w + \frac{\int_{r_{\min}}^{r_{\max}} dn(r)/dr \cdot C_{bk}(r) v_f(r) dr}{\int_{r_{\min}}^{r_{\max}} dn(r)/dr \cdot C_{bk}(r) dr}, \quad (3)$$

where w is the vertical wind velocity and v_f is the terminal falling velocities of hydrometeors particles. In this radar-signal simulator, v_f is calculated in the form of $v_f(r) = -V_t(r)\sqrt{p_0 / p}$, where p is the pressure and the variable with subscript 0 stands for the standard reference pressure set at 1000 hPa, and V_t is the terminal fall velocities of hydrometeros particles at p_0 dependent on the size and type [*Khain and Sednev*, 1995].

2.3 Cloud radar observations

2.3.1 MR01/K02 cruise of the research vessel MIRAI

The MR01/K02 research cruise was conducted with ship-borne 95 GHz Doppler radar and lidar of zenith looking over the northwest Pacific near Japan from 14 to 28

May 2001 [*Sugimoto et al*., 2002; *Okamoto et al*., 2007]. This observation provided the dataset products of variables such as factor Ze, the linear depolarization ratio (LDR), DV, and the correlation coefficient between the horizontal and vertical signals; the technical description can be found in *Horie et al*., [2000]. The vertical range of the data was to a height of approximately 12 km with intervals of 82.5 m with a time resolution of 1 minute. This study targets only 22 and 23 May 2001, when the vessel stayed around 146°E, 34°N and a mid-latitude low-pressure system with associated fronts westerly approached and passed over the vessel (Figure 1 (a)). The radar observed the vertical structure of cloud and precipitation attributable to the low-pressure and frontal system. Passing clouds were generally composed of altostratus, nimbostratus and shallow cumulus.

2.3.2 CloudSat CPR observation

The CloudSat with a space-borne 94 GHz CPR of nadir looking is a polar-orbiting satellite with a mean equatorial altitude of 705 km in the formation of the five satellites known as the A-train constellation [*Stephens* 2002; *Stephens et al*., 2008]. The vertical range resolution of the CPR data is 485 m, and the horizontal cross-track and along-track resolutions are 1.4 km and 1.8 km, respectively. The dBZe data in the CloudSat 2B-GEOPROF product [*Mace et al*., 2007; *Stephens et al*., 2008, Table 2] is provided from the CloudSat Data Processing Center (DPC).

We analyzed two cases when CloudSat passed over clouds around the Japan on 11 and 14 November 2006 with dissimilar weather conditions and regions. The corresponding CloudSat track granules were numbered 2873 and 2917 by the CloudSat DPC, respectively. In the first case, the satellite passed over the northeastern part of the Japan at nearly 1638 universal time (UTC) on 11 November from 141.7°E, 34.6°N to 145.7°E, 46.1°N (these latitude and longitude boundaries followed those of the QuickLook segment shown by the DPC). The CPR observed the very thick nimbostratus and precipitation located near the center of a low-pressure system in the mature stage (Figure 1 (b)). In general, settled vertical structure of reflectivity extended from 39°N to 46°N along the footprint of the satellite. In the second case, the satellite passed over the Japan Sea generally at 1708 UTC on 14 November from 134.0°E, 34.6°N to 137.6°E, 46.1°N. The CPR observed the structure of shallow convective clouds extending behind a cold front over the sea surface (Figure 1 (c)).

3. Results

3.1 Setup of Numerical Experiments

Three sets of NWP simulations were prepared for 22-23 May 2001, and 11 and 14 November 2006 (hereinafter, these three cases are referred to as M2223, C2873, and C2917). The simulation domains for M2223, C2873, and C2917 were centered at 146°E-34°N, 143°E-42°N, and 135°E-38°N, respectively. The domain for all cases had a horizontal scale of 600 km with a grid interval size of 3 km. The vertical grid component to a height of 22600 m was divided into 40 layers with intervals increasing from 40 m to 1120 m with altitude. A time step of 20 sec was set for the calculation of dynamics; a variable time step shorter than it was applied for that of cloud microphysics.

The JMA mesoanalysis dataset (JMA-MANAL) with horizontal grid interval of 10 km, 20 vertical layers, and 4 samples for 2001 and 8 samples for 2006 per day, was employed for the NWP simulation to set the initial and lateral boundary conditions of prognostic variables (i.e. two components of horizontal velocities, potential temperature, and mixing ratio of water vapor). The National Centers for Environmental Prediction (NCEP) Reanalysis data with a horizontal resolution of T62 Gaussian grid and 4 samples per day was employed to set sea surface temperature (SST). Condensation nuclei (CN) nesting procedure [*Iguchi et al*., 2008] is applied for the simulation; the CN fields were calculated from the spectral radiation transport model for aerosol species (SPRINTARS) [e.g. *Takemura et al.*, 2005] coupled with the Center for Climate System Research/National Institute for Environmental Studies Atmospheric General Circulation Model (CCSR/NIES-AGCM) [*K-1 model developers*, 2004] simulation with a horizontal resolution of T106 Gaussian grid, 20 vertical layers, and 1 sample per day.

In the case of M2223, the nine individual NWP simulations for 6 hours integration were conducted from 1800 UTC on 21 May to 2400 UTC on 23 May 2001; a simulation transferred the some prognostic variables (i.e. potential temperature, mixing ratio of vapor, and PSDs of hydrometeors particles and CN) to the next simulation by way of its initialization. Prognostic variables in the column over the horizontal grid nearest to the coordinates of the vessel were continuously sampled per 1 minute during the two days. In the cases of C2873 and C2917, the two simulations for 6 hours integration were conducted from 0600 UTC to 1800 UTC on 11 and 14 November 2006, respectively. Prognostic variables in the columns over the nearest horizontal grids to the footprints of CloudSat were sampled in the forms of snapshots at 1638 UTC on 11 and at 1708 UTC on 14 November.

3.2 Comparison with the W-band radar observations

3.2.1 MIRAI ship-borne Doppler radar (M2223)

Figure 2 illustrates the time-height cross sections (THCSs) of dBZe measured by the 95 GHz radar and calculated through the radar-signal simulator offline-coupled with the bin and bulk model simulations for the period of 24 hours from 1200 UTC on 22 to 1200 UTC on 23 May 2001. Upper ice clouds and shallow warm clouds persistently lasted, and the cloud layers and precipitation from the ice cloud are mainly observed. Some Ze discontinuity in the direction of time axis resulted from the redome correction. The first half of 22 May and the second half of 23 May were not included in this analysis, because few clouds existed during the first half of 22nd, and the radar data was excluded from the product due to heavy precipitation during the second half of 23rd.

The ice and water hydrometeors layers were partitioned at the height of approximately 4 km. This freezing level was also estimated from the temperature profile in the model simulation and the profile of LDR measured by the ship-borne radar (now shown); LDR profile highlighted freezing level with the maximum value. Under 4 km in Figure 2, both the simulations reasonably reproduced the magnitude and distribution of observed dBZe in general. The agreement between the observation and the bin model simulation is better than with the bulk model simulation; that shows a probability for the bin model simulation to reproduce the PSD of liquid hydrometeors representative of cloud microphysics within the layer, which was composed of shallow water clouds and precipitation from upper ice clouds. Whereas, the dBZe calculated through the bulk model simulation promises to be improved by a tuning of the BIF. Turning to ice cloud layer from 4 km to 9 km, the comparison highlights overestimation of dBZe calculated from the bin model simulation. In contrast, the bulk model simulation reproduced almost the same magnitude of observed dBZe, which meant that the BIF was suitable to represent dBZe for ice particles in this case.

Figure 3 shows a qualitative comparison in the form of normalized contoured-frequency-by-altitude diagrams (CFADs) of dBZe [e.g. *Stephens et al.*, 2008, Figure

15]. The CFADs in the observation and the bin model simulation are generally in agreement, especially in the water layer under approximately 4 km. However, overestimation is still highlighted within an altitude range from 4 km to 9 km as shown in Figure 2; the difference in the maximums of dBZe within the altitude range is approximately 10 dB. The CFAD of the bulk model case is generally similar to those under 4 km in the observation and in the bin model case. Over the height, the profiles of CFAD are different however; the contoured area of high frequency is small in spread, and a weak relationship between height and dBZe is shown compared to those in both the observation and the bin model cases. This lack of spread is due to an application of single-moment bulk scheme with an assumption of BIF to the simulator [*Bodas-Salcedo et al*., 2008], whereas the weak height-dBZe relationship is caused by no dependence of BIF on temperature. In contrast, the spread is sufficiently wide in CFAD of the bin model simulation, suggesting that the utilization of prognostic PSD results in a better dBZe simulation.

Ze-LWC and Ze-IWC correlations are principal aspects representative of cloud microphysics. The relationships are influenced by cloud microphysical processes deciding PSDs of water and ice particles. For example, coalescence growth conserves the LWC or IWC but changes the Ze, whereas diffusion or deposition growth brings increases in both. Figure 4 shows the Ze-LWC relationships in the model simulations in the form of normalized contoured frequency by logarithmic LWC diagram (CFLD); note that Ze in these figures was corrected not to include attenuation by atmospheric hydrometeors and environment of the instrument. The figure clearly illustrates the substantial difference in the warm cloud microphysics of both the simulations. The profile of CFLD from the bin model simulation (Figure 4 (a)) is like a portion of a parallelogram. In contrast, in Figure 4 (b) a corresponding portion of a parallelogram is lacked within lower LWC range nearly less than 10^{-4} g/m^3, and the right-end diagonal line of profile is significantly clear but the left-end diagonal line disappears. This characteristic difference can be mainly attributed to the instantaneous saturation adjustment applied in the bulk microphysics. Cloud water instantaneously evaporates and cannot exist at sub-saturated grid points, whereas rain water may remain although it evaporates at a characteristic rate for time. The diagonal lines at both left and right ends of the parallelogram in Figure 4 (a) are approximately corresponding to the Ze-LWC relations of only small and large radius droplets in the bin microphysics, respectively. In contrast, both the equivalent diagonal lines in Figure 4 (b) are definitely corresponding to the Ze-LWC relations of the categorized cloud water and rain modes in the bulk microphysics, respectively; Ze anywhere between the diagonal lines can be represented by the average of Ze values from cloud water and rain modes. Since cloud water cannot stay at the sub-saturated grid where LWC is probably not very large, Ze within the lower LWC range tends to be concentrated on the right-side diagonal line corresponding to the Ze-LWC relation only from the rain mode. This characteristic often appeared in a sub-saturated zone just under an ice cloud with melted precipitation. That results in the contoured area of high frequency in Figure 3 (c) smaller in width than in Figure 3 (b), especially just under a height of approximately 4 km.

Figure 5 shows Ze-IWC relationships from the model simulations in the form of normalized contoured frequency by logarithmic IWC diagram (CFID), showing a strong linear relationship of Ze-IWC compared to Ze-LWC in both the simulations.

Thus IWC is a principal parameter to decide Ze under the linear relationship. Turning to a discussion of the perspective above for Figure 4, the diagonal lines at both sides of the contoured profile in Figure 5 (a) approximately mean that the two Ze-IWC relations are attributed to small and large radius ice particles (inclusive of ice crystals, snowflakes, graupels, or hails), respectively; however the difference in both the Ze-IWC relations is not large. Thus the feature of CFID in Fig 4 (a) means a monotonous structure in a radius of ice particles in the bin model simulation. Whereas the diagonal lines at both sides of the profile in Figure 5 (b) are definitely corresponding to the Ze-IWC relations of the cloud ice and snow-graupel modes in the bulk model simulation, although the left-side line almost disappear. It is attributed to the similarity in the BIFs applied to PSDs of snow and graupel modes and the scarcity of cloud ice mode.

As shown in Figure 3, a main problem in the reproducibility of dBZe is the overestimation in ice cloud layer of the bin model simulation. Three causes can be indicated for the source: problems of the Ze-IWC relationship, an overestimation of IWC, and/or modeling of attenuation effect. At beginning, empirical Ze-IWC relations were used to check the validity by the comparison with this model simulation. Many empirical Ze-IWC relations were reported by prior studies such as with ground-based or airborne direct sampling using a W-band radar and a probe, and with an application of a scattering theory to PSD derived from an observation or a cloud resolving simulation [e.g. *Sassen et al.*, 2002]. Figure 6 shows the scatter plot diagram of Ze-IWC from this bin model simulation with overlaid lines showing empirical relations derived from other studies [*Sassen and Liao*, 1996; *Heymsfield et al.*, 2005; *Okamoto et al.*, 2007]: $IWC=0.086Ze^{0.83}$ [*Sassen and Liao*, 1996; *Sassen et* *al*., 2002] was derived from a regression analysis for IWC and Ze computed from PSD of precipitating ice crystals measured by ground-based observation in South Pole station in Antarctica [*Sato et al*., 1981]. $IWC=0.675Ze^{0.64}(Ze < 0.0032$ $\mathrm{mm}^6/\mathrm{m}^3)$, $IWC=0.194Ze^{0.42}(0.0032 < Ze < 3.97\ \mathrm{mm}^6/\mathrm{m}^3)$, and $IWC=0.224Ze^{0.32}(Ze >$ $3.97\ \mathrm{mm}^6/\mathrm{m}^3)$ [*Heymsfield et al*., 2005] were obtained from a sectional regression analysis for IWC and Ze computed from PSD massively sampled by the aircraft with an impactor probe during Cirrus Regional Study of Tropical Anvils and Cirrus Layers Florida Area Cirrus Experiment (CRYSTAL-FACE) over southern Florida during July 2002 [*Heymsfield* et al., 2004]. $dBZe=\{\log_{10}(IWC)+0.93949\}/0.0706$ [*Okamoto et al*., 2007, Equation 5] was derived in the modified form of the relationship from *Hogan and Illingworth* [1999] and *Hogan et al*. [2001]; they derived it from an application of least-squares fitting to radar reflectivity factor (Z) and $\log_{10}$(IWC) computed from PSD in mid-latitude aircraft measurements during European Cloud Radiation Experiment in September and October 1993 (EUCREX'93) took place in Scotland. (hereinafter, their empirical relationships are referred to as SL96, HE05, and OK07 in order.)

In Figure 6, the crowd of scatter plots from this simulation is clearly shifted to larger dBZe compared to the lines of empirical relations derived from the other studies. Thus a poor simulation of Ze-IWC relation is considered as a source of the Ze overestimation. Note that Figure 6 also shows the Ze-IWC relation using the Ze simulator for the ice clouds assumed to be only composed of snowflakes of the radius approximately 100 microns. This relation line can be a reference to consider a bias suitable to the empirical relations in using the Ze simulator. Thus the empirical relations are not necessarily irreproducible in this simulator. In fact, the simulated effective ice radii are roughly 200 microns under a height of 9 km, and partially over 400 microns (Figure 7).

Figure 8 shows the THCSs of dBZe (similar to Figure 2 (b)) in the bin model simulation with the direct applications of HE05 and OK07 relationships to the simulated IWC instead of using the Ze simulator for ice clouds (the attenuation is the same). These new THCSs are clearly in agreement with those in the observation (Figures 2 (a) and 3 (a)); the overestimation of Ze in the ice cloud layer has been solved, although a slight underestimation newly occurs in the case of HE05. This better agreement in the case of OK07 than HE05 may be caused by the difference in reference latitudes of the studies. Also note that the better reproducibility in the bulk model simulation is probably due to the assumption of mean radii set as nearly 100 microns.

This result with the empirical Ze-IWC relations suggested probability of improving the reproducibility through modification of Ze-IWC in the simulation. First of all, smaller backscattering cross section and optical thickness of snowflakes were applied for the radar simulator under the same IWC; both the corresponding parameters are calculated on the assumption that the mass equivalent radius is decreased to the half (Figure 9). The agreement between the simulation and observation profiles is better, especially small discontinuity around the freezing level is reproduced. However, which physical factor actually causes the overestimation is still a matter of debate. Note that the ice density of 0.9 g/cm^3 is used now, so that no scope for an increase in the density attributable to a smaller radius to reduce the reflectivity.

A trial simulation was conducted to probe a possibility of improvement in the reproducibility by a tuning and to specify the source of the problem. In this simulation, large snowflakes were set to forcibly break-up into small ones: all snowflakes with radius larger than about 750 microns were impartially converted to about 550 microns snowflakes, and snowflakes with radius about from 130 to 550 microns were partly transferred to the next smaller size bins in conservation of mass. As a result, effective ice radius was kept below approximately 200 microns (not figured), and the overestimation of dBZe in ice cloud layer was canceled in this trial simulation (Figure 10 (a) and (b)). Figure 10 (c) shows the scatter plot diagram of Ze-IWC from this trial simulation with the crowd of plots shifting to smaller dBZe compared to that in Figure 6 and in better agreement with the lines of the empirical relations.

To consider the problem from other viewpoint, Doppler velocity (DV) is focused, hereinafter. Figures 11 and 12 illustrate the THCSs and their CFADs of radar-observed and model-simulated DVs shown only on vertical areas of the dBZe larger than –20 dB, respectively. The observed DV is slightly larger than in the simulation generally; the observed DV spectrum is wider over the freezing level, approximately 4 km in the CFADs. It may be proper to implicate this DV difference in the Ze difference and furthermore the overestimation of model-simulated Ze. Small falling velocity of ice particles is likely to cause inefficiency for those to fall out from the ice cloud layer. Single modes are dominant over the freezing level in both the CFADs, in contrast double modes appear under the freezing level. The large DV mode corresponds to the precipitation from upper ice clouds over the freezing level, whereas the small mode corresponds to warm clouds whose cloud tops do not reach the freezing level. The weak dominance of large DV mode in the model-simulated case was probably attributed to inefficient precipitation, compared to the observed real case. This large DV mode completely disappeared in the trial simulation with the forcible breakup of snowflakes (Figure 13) because of no precipitation from melted large snowflakes. This contradiction in features between agreement of Ze and disagreement of DV suggested that the plane tuning with cutting large-size snowflakes could not bring an essential solution to the problem; the large-size snowflakes are necessary for the reproducibility of DV.

Further trial simulations were conducted to investigate sensitivity of model-simulated DV and Ze to the terminal fall velocities of ice hydrometeors. The sensitivity simulation was set as follows: the terminal velocities of all ice hydrometeors were equalized to those of droplets in all bins. The terminal fall velocity of each hydrometeor at standard pressure (1000 hPa) is summarized in Figure 14, with the velocities of droplets the largest, and those of hails the next largest at least within the range over than 1 m/s.

An increase in falling velocities of ice hydrometeors led a decrease in dBZe through a decrease in IWC, suggested from THCSs and CFADs of dBZe and DV in the trial simulations as illustrated in Figure 15 and THCSs of IWC shown in Figure 16. As a result, the profile of dBZe in this trial simulation got more similar to those of dBZe in the observation (Figures 2 (a) and 3 (a)), but an overestimation of DV newly arose. After all the reproducibility of DV was not so poor as the overestimation of dBZe was completely offset. The Ze-IWC relationship in this trial simulation still unmatched with the lines of empirical relations with larger dBZe, especially in the part of large IWC (Figure 17), similar to that of the original simulation except for with smaller IWC range.

3.2.2 CloudSat space-borne CPR (C2873 and C2917)

The comparison with CloudSat CPR observation may bring another point of view to the issue. Attenuation by atmospheric component is integrated from the zenith without redome correction, so that upper ice clouds can be seen almost without attenuation.

The dBZe profiles were highlighted for C2873 and C2917 (Figures 18 and 19, respectively), in the form of the latitude-height cross sections (LHCSs) of dBZe measured by the CloudSat CPR and calculated using the bin model simulation. The freezing level was approximately located at the heights of 2 km in both cases, and the overestimations of dBZe in ice cloud layers were seen also. This result suggested that an error in the modeling of attenuation was not a source of the dBZe overestimation.

The results of sensitivity simulations were also highlighted in Figures 18 and 19, whose settings were the same as used in the case of M2223. Different from the M2223 case, the graphs using the OK07 relationship are not the most consistent with those of the observation, especially in case of C2873 (Figure 18 (c)). On the other hand, the same setting as Figure 15 (where the terminal velocities of all ice hydrometeors were equalized to those of droplets in all bins) brought about better results in their sensitivity simulations.

In case of C2873, the model simulation reproduced the general features of extended thick nimbostratus except for invisible precipitation in the lower layer under 2 km. In fact, the model predicted precipitation under the freezing level, but strong attenuation in the upper ice clouds made it invisible. Since the same magnitude of attenuation was used to plot Figure 18 (c), the dBZe profile was underestimated compared to the observation. This large attenuation indicated a possibility of overestimations of extinction efficiency factor, of IWC, and/or of particle radii resulting in large optical thickness at the wavelength. Figures 18 (d) and (e) illustrated precipitation more visible in the sensitivity simulations because of less optical thickness due to a decrease in ice radii (Figure 18 (d)) and IWC (Figure 18 (e)). In particular, Figure 18 (e) showed layers of second maximum of dBZe just under the melting level around 2 km, which were confirmed in the observation. Figure 18 (f) illustrated dBZe profile from the same result as in Figure 18 (e) except for using the OK07 Ze-IWC relation; the profile became in better agreement even though some underestimation in ice clouds layer.

In case of C2917 similarly, the dBZe profile of the model simulation was in agreement with that in the observation except for overestimations of IWC and cloud top height in the northern part. A strong attenuation was not seen in the shallow convective clouds because the IWC was not very large, although discontinuity of Ze appeared near the melting level at the height of 2 km. Different from the case of C2917, both Figures 19 (c) and (e) showed good reproducibility.

3.2.3 Summarized discussion of the overestimation of reflectivity in ice clouds

Up to here the issue of reproducibility on the bin model simulated dBZe was investigated based on the comparisons with the ship-borne and space-borne observations individually. This subsection would suggest a discussion of the problem. The main common problem was an overestimation of dBZe in ice cloud layers over freezing levels attributable to problems of erroneous Ze-IWC relationship and/or an overestimation of IWC. Some sensitivity test simulations and an application of the empirical Ze-IWC relation suggested better results.

Two speculations are offered on the source of erroneous Ze-IWC relationship. One is a bias in the calculation of the Ze simulator, which is biased to larger dBZe compared to the empirical relationships and hence caused the overestimation of dBZe in ice cloud layers. Another is an overestimation of IWC on the assumption that the empirical Ze-IWC relationships are inadequate for our cases. A trial simulation suggested that the problem could have been associated with large sizes of snowflakes, but they were necessary for producing large fall velocity of melted precipitation from ice clouds.

Some problems remain conjectural and the verification would be further research topics: The present assumptions of nonsphericity, inhomogeneousity, and density of ice particles still produce a large uncertainty in the radar-signal simulator. In particular, the potential error due to such factors is bigger for large-size ice particles [e.g., *Sato and Okamoto*, 2006]. Furthermore, the present cloud microphysical model is optimized to calculate physical properties, whereas it is insufficient to calculate changes in radiative properties resulting from microphysical processes even though PSD is directly substituted. Prior studies [e.g. *Sassen et al*., 2002] showed that an explicit cloud microphysical model could produce results fitting the observation data. Thus, there is plenty of improvement even in the present model specification. For example, a problem is the size range covered by the present microphysical scheme. The increase in terminal fall velocities of ice particles do not terminate at the particle size of largest bin (Figure 14). If the bins cover a larger size range, IWC may be decreased as a result of an increase in fall velocities on average although a mean particles size increases.

Evaluation of IWC is important to decide the source of the problem. The sensitivity test simulation with the change of DV showed improvement in reproducibility of dBZe profiles as a result of change of IWC. However the reproducibility of DV was not so poor as the overestimation of dBZe was offset, and hence other factors should be suggested. IWC can change by dynamical and microphysical factors, and initial/boundary conditions. An amount of deposition from supersaturation to IWC is strongly dependent on the ice cloud microphysics [e.g. *Khvorostyanov and Sassen*, 1998a; 1998b; *Hashimoto et al.*, 2007]; supersaturation over ice is not canceled immediately and can remain at certain percentages, which is different from supersaturation over water. In fact, high supersaturation larger than 10 % over ice was simulated in the present simulations for the case studies. No methods directly validate supersaturation or deposition from vapor to ice, so that we cannot discuss a solution to the problem now. Figure 16 (c) shows THCS of IWC in the bulk model simulation; its maximums in the segment was more similar to Figure 16 (b) than Figure 16 (a). The better reproducibility in the bulk model simulation might be attributed to this feature besides the assumption of mean radii in BIF. The disparity in IWC in the bin and bulk model is due to differences not only in how to calculate terminal falling velocities but also in their microphysics.

Modeling of attenuation effect is an uncertain factor and would be added to the discussion about dBZe of ice clouds. The Ze overestimation was seen in both ship-borne and space-borne cases. We thus suppose that errors in the attenuation modeling were not involved in the Ze overestimation, although it is impossible to evaluate the validity of attenuation modeling using the present available data. Whereas very large optical thickness in ice clouds layer in the CloudSat case is clearly unreasonable. This can be interpreted as a result of the bias in the Ze simulator or the overestimation of IWC, but still should be controversial issue._On the other hand, redome correction should be noticed in the ship-borne case because 9 dB subtraction in the present correction is approximately equivalent to the magnitude of overestimation of dBZe in the ice clouds. We conducted the Ze simulation assuming that 9 dB is subtracted regardless of precipitation amount as redome correction applied for the whole period of time (not figured). As a result, the overestimation was canceled in general, but an underestimation newly occurred approximately under 4 km. This result in the lower part does not agree with the observation, so that it seems to us that the present poor modeling of redome correction does not cause the overestimation of dBZe.

4. Conclusions

In this paper, we conducted three case studies with NWP simulations using a meso-scale model coupled with SBM to be compared with W-band ship-borne and space-borne radar observations. A radar-signal simulator was applied to the simulation results for a direct comparison on the radar-signal product basis. The comparison showed that the simulated Ze and Doppler velocity profiles were generally in agreement with those of the observations. In particular, proper diversity of Ze was simulated, which was not reproduced in the bulk model simulation. However, an overestimation of Ze in upper ice clouds layers was a major problem in the reproducibility. The reason was searched for by conducting sensitivity test simulations and referring to empirical Ze-IWC relationships. A strong linear correlation between Ze and IWC was seen and hence IWC was a principal parameter to decide Ze in the model simulation. As compared with the empirical relationships, the scatter plots of simulated Ze-IWC was shifted to larger Ze side. Thus, the disagreement on the Ze-IWC relationships can be a key factor of the Ze overestimation. On the other hand, the comparison of DV suggested that the large sizes of snowflakes are necessary for enough precipitation under the freezing level. Based on the results of sensitivity simulations, we concluded that the source of the problem is a bias in the calculation of the Ze simulator or an overestimation of IWC on the assumption that the empirical Ze-IWC relationships are not applicable to the cases of this study. It is difficult to judge which factors or both are actually attributed to the problem from the discussion with the present data.

A further observation using a multi-wavelength remote sensing is required in order to investigate the issue. Lidar observations are often accompanied by W-band radar observations, for example CALIPSO with CloudSat and lidar at 532 and 1064 mm wavelengths on board of MIRAI. Their observations for clouds, however, are unsatisfactory because the entire profile of cloud often cannot be seen due to a strong attenuation at the wavelengths. X band frequencies is widely used together with W-band frequency, TRMM/PR is representative [e.g., *Masunaga et al.*, 2008]. Whereas K-band multi-wavelength radar or radiometer are also utilized to observe clouds on site [e.g., *Illingworth et al.*, 2007]. In addition, some recent papers also reported the overestimation of the radar reflectivity due to snow or graupels [*Eito and Aonashi*, 2009; *Li et al.*, 2009]; the common model framework or scheme are used in their and this researches. A follow-up study of these papers using our model and radar-signal simulator is significantly useful for investigating the issue.

Acknowledgement

This study was supported by projects of JAXA/EarthCARE, MEXT/VL for Climate System Diagnostics, MOE/Global Environment Research Fund B-083, NIES/GOSAT, and JST/CREST. One of the authors (A. Khain) is supported by a grant from the Israel Science Foundation (140/07). The authors wish to acknowledge the developers of the JMA-NHM and HUCM. We also thanks the persons concerned JAMSTEC for conducting the observation mission on the Research Vessel MIRAI. CloudSat products were come by from the CloudSat Data Processing Center; this processing was supported by Toshiro Inoue of Center for Climate System Research.

Reference list

Austin, R.J., A.J. Heymsfield and G.L.Stephens (2008), Retrievals of ice cloud microphysical parameters using the CloudSaat millimeter wave radar and temperature, submitted to J. Geophys. Res., in press.

Clothiaux, E., M. Miller, B. Albrecht, T. Ackerman, J. Verlinde, D. Babb, R. Peters, and W. Syrett (1995), An Evaluation of a 94-GHz Radar for Remote Sensing of Cloud Properties. J. Atmos. Oceanic Technol., 12, 201–229.

Bodas-Salcedo, A., M. J. Webb, M. E. Brooks, M. A. Ringer, K. D. William, S. F. Milton, and D. R. Wilson (2008), Evaluating cloud systems in the Met Office global forecast model using simulated CloudSat radar reflectivities, J. Geophys. Res., 113, D00A13, doi:10.1029/2007JD009620.

Eito H., and K. Aonashi (2009), erification of hydrometeor properties simulated by a cloud-resolving model using a passive microwave satellite and ground-based radar observations for a rainfall system associated with the Baiu front, JMSJ, 87A, 425-446, doi:10.2151/jmsj.87A.425.

Hashimoto A., M. Murakami, T. Kato and M. Nakamura (2007), Evaluation of the influence of saturation adjustment with respect to ice on meso-scale model simulations for the case of 22 June, 2002. SOLA, 3, 85-88, doi:10.2151/sola.2007-022.

Haynes, J., R. T. Marchand, Z. Luo, A. Bodas-Salcedo, and G. L. Stephens (2007), A Multipurpose Radar Simulation Package: QuickBeam, Bull. Amer. Met. Soc., 88, 1723–1727.

Heymsfield, A. J., A. Bansemer, C. Schmitt, C. Twohy, and M. R. Poellot (2004), Effective ice particle densities derived from aircraft data. J. Atmos. Sci., 61, 982–1003.

Heymsfield, A. J., Z. Wang, and S. Matrosov (2005), Improved radar ice water content retrieval algorithms using coincident microphysical and radar measurements. J. Appl. Meteor., 44, 1391–1412.

Hogan, R. J., and A. J. Illingworth (1999), The potential of spaceborne dual-wavelength radar to make global measurements of cirrus clouds. J. Atmos. Oceanic Technol., 16, 518–531.

Hogan, R. J., C. Jakob, and A. J. Illingworth (2001), Comparison of ECMWF winter-season cloud fraction with radar derived values, J. Appl. Meteorol., 40(3), 513– 525.

Horie, H., T. Iguchi, H. Hanado, H. Kuroiwa, H. Okamoto, and H. Kumagai (2000), Development of a 95-GHz airborne cloud profiling radar (SPIDER): Technical aspects, IEICE Trans. Commun., E83-B(No. 9), 2010–2020.

Ikawa, M., and K. Saito (1991), Description of a non-hydrostatic model developed at the Forecast Research Department of the MRI, Tech. Rep. MRI, 28, 238 pp., Meteorol. Res. Inst., Tsukuba, Japan.

Iguchi, T., T. Nakajima, A. P. Khain, K. Saito, T. Takemura, and K. Suzuki (2008), Modeling the influence of aerosols on cloud microphysical properties in the east Asia region using a mesoscale model coupled with a bin-based cloud microphysics scheme, J. Geophys. Res., 113, D14215, doi:10.1029/2007JD009774.

Illingworth, A. J. and et al. (2007), Continuous evaluation of cloud profiles in seven operational models using ground-based observations, Bull. Amer. Meteor. Soc., 88, 883-898.

Inoue, T., Satoh, M., Hagihara, Y., Miura, H., and Schmetz, J. (2009), Comparison of high-level clouds represented in a global cloud-system resolving model with CALIPSO/CloudSat and geostationary satellite observations., J. Geophys. Res., accepted.

K-1 model developers, K-1 coupled model (MIROC) description (2004), K-1 Technical Report, vol. 1, H. Hasumi and S. Emori (eds.), Center for Climate System Research, University of Tokyo, 34 pp.

Khain, A. P., and I. L. Sednev (1995), Simulation of hydrometeor size spectra evolution by water-water, ice-water and ice-ice interactions, Atmos. Res., 36, 107–138, doi:10.1016/0169-8095(94)00030-H.

Khain, A. P., M. Ovtchinnikov, M. Pinsky, A. Plkrovsky, and H. Krugliak (2000), Notes on the state-of-the-art numerical modeling of cloud microphysics, Atmos. Res., 55, 159–224, doi:10.1016/S0169-8095(00)00064-8.

Khvorostyanov, V. I. and K. Sassen (1998), Cirrus cloud simulation using explicit microphysics and radiation. Part I: Model description. J. Atmos. Sci., 55, 1808-1821.

Khvorostyanov, V. I. and K. Sassen (1998), Cirrus cloud simulation using explicit microphysics and radiation. Part II: Microphysics, vapor and ice mass budgets, and optical and radiative properties. J. Atmos. Sci., 55, 1822-1845.

Lhermitte, R. (1987), A 94-GHz Doppler Radar for Cloud Observations. J. Atmos. Oceanic Technol., 4, 36–48.

Li, X., W. Tao, T. Matsui, C. Liu, and H. Masunaga (2009), Improving a spectral bin microphysical scheme using TRMM satellite observations, Q. J. R. Meteorol. Soc., accepted.

Lin, Y. H., R. D. Farley, and H. D. Orville (1983), Bulk parameterization of the snow field in a cloud model. J. Climate Appl. Meteor., 22, 1065–1092.

Mace, G. G., R. Marchand, Q. Zhang, and G. Stephens (2007), Global hydrometeor occurrence as observed by CloudSat: Initial observations from summer 2006, Geophys. Res. Lett., 34, L09808, doi:10.1029/2006GL029017.

Marchand, R. T., Mace, G. Ackerman, T. and Stephens, G. (2007), A Comparison of CloudSat Cloud Radar Observations with Simulated Cloud Radar Output from the Multiscale Modeling Framework Global Climate Model. J. Geophys Res., in press.

Masunaga, H., M. Satoh, and H. Miura (2008), A joint satellite and global cloud-resolving model analysis of a Madden-Julian Oscillation event: Model diagnosis, J. Geophys. Res., 113, D17210, doi:10.1029/2008JD009986.

Miura, H., M. Satoh, T. Nasuno, A. T. Noda, and K. Oouchi (2007), A Madden-Julian Oscillation event realistically simulated by a global cloud-resolving model, Science, 318, 1763 – 1765, doi:10.1126/science.1148443.

Okamoto, H. (2002), Information content of the 95 GHz cloud radar signals: Theoretical assessment of effects of non-sphericity and error evaluations of the discrete dipole approximation, J. Geophys. Res., 107(D22), 4628, doi:10.1029/2001JD001386.

Okamoto, H., et al. (2007), Vertical cloud structure observed from shipborne radar and lidar: Midlatitude case study during the MR01/K02 cruise of the research vessel Mirai, J. Geophys. Res., 112, D08216, doi:10.1029/2006JD007628.

Saito, K., et al. (2006), The operational JMA nonhydrostatic mesoscale model, Mon. Weather Rev., 134(4), 1266, doi:10.1175/MWR3120.1.

Sassen, K. and L. Liao (1996), Estimation of cloud content by W-band radar. J. Appl. Meteor., 35, 932–938.

Sassen, K., Z. Wang, V. I. Khvorostyanov, G. L. Stephens, and A. Bennedetti (2002), Cirrus cloud ice water content radar algorithm evaluation using an explicit cloud microphysical model. J. Appl. Meteor., 41, 620–628.

Sato, N., K. Kikuchi, S. C. Barnard, and A. W. Hogan (1981), Some characteristic properties of ice crystal precipitation in summer season at South Pole Station, Antarctica, J. Meteor. Soc. Japan, 59, 772-780.

Sato, K., and H. Okamoto (2006), Characterization of Ze and LDR of nonspherical and inhomogeneous ice particles for 95-GHz cloud radar: Its implication to microphysical retrievals, J. Geophys. Res., 111, D22213, doi:10.1029/2005JD006959.

Satoh, M., Inoue, T., and Miura, H. (2009), Evaluations of cloud properties of global and local cloud-system resolving models using CALIPSO/CloudSat simulators., J. Geophys. Res., accepted.

Sekiguchi, M., and T. Nakajima (2008), A k-distribution-based radiation code and its computational optimization for an atmospheric general circulation model, Journal of Quantitative Spectroscopy and Radiative Transfer, 109, 17-18, November-December 2008, 2779-2793, DOI: 10.1016/j.jqsrt.2008.07.013.

Seifert, A. and K. D. Beheng (2006), A two-moment cloud microphysics parameterization for mixed-phase clouds. Part 1: Model description, Meteorol. Atmos. Phys., 92, 45-66.

Stephens, G. L., et al. (2002), The CloudSat mission and the A-Train, Bull. Am. Meteorol. Soc., 83, 1771–1790.

Stephens, G. L., et al. (2008), The CloudSat mission: Performance and early science after the first year of operation, J. Geophys. Res., 113, D00A18, doi:10.1029/2008JD009982.

Sugimoto, N., I. Matsui, A. Shimizu, I. Uno, K. Asai, T. Endoh, and T. Nakajima (2002), Observation of dust and anthropogenic aerosol plumes in the Northwest Pacific with a two-wavelength polarization lidar on board the research vessel Mirai, Geophys. Res. Lett., 29(19), 1901, doi:10.1029/2002GL015112.

Takemura, T., T. Nozawa, S. Emori, T. Y. Nakajima, and T. Nakajima (2005), Simulation of climate response to aerosol direct and indirect effects with aerosol transport-radiation model, J. Geophys. Res., 110, D02202, doi:10.1029/2004JD005029.

Woods, C. P., D. E. Waliser, J.-L. Li, R. T. Austin, G. L. Stephens, and D. G. Vane (2008), Evaluating CloudSat ice water content retrievals using a cloud-resolving model: Sensitivities to frozen particle properties, J. Geophys. Res., 113, D00A11, doi:10.1029/2008JD009941.

Yamada, Y. (2003), Cloud microphysics (in Japanese), in The JMA Nonhydrostatic Model, Annu. Rep., 49, pp. 52– 76, Jpn. Meteorol. Agency, Tokyo.

Figure captions

Figure 1. Surface weather charts (a) at 0000 UTC on 23 May 2001, (b) at 1200 UTC on 11 November 2001, and (c) 1200 UTC on 14 November 2001, with overlaid black squares corresponding to the simulation domains and green dot and lines denoting the rough coordinates of the MIRAI and footprints of the CloudSat, respectively. (These surface weather charts produced by Japan Meteorological Agency)

Figure 2. Time height cross-sections (THCS) of the equivalent radar reflectivity factor dBZe (a) measured by the 95 GHz Doppler radar on board of the MIRAI, and calculated by the radar-signal simulator applied to the results of (b) bin and (c) bulk model simulations from 1200 UTC on May 22 to 1200 UTC on May 23 2001.

Figure 3. Normalized contoured-frequency-by-altitude diagrams (CFADs) of dBZe constructed from (a) the measurement on MIRAI, and the simulations by (b) bin and (c) bulk model during the same period as Figure 2.

Figure 4. Normalized contoured-frequency-by-LWC diagrams (CFLDs) of dBZe constructed from the (a) bin and (b) bulk model simulations.

Figure 5. Same as Figure 4 but for frequency-by-IWC (CFIDs).

Figure 6. Scatter plots and relationship lines between Ze and IWC diagrams. Black dots depict Ze-IWC plots in the bin model simulation, and blue line is a crowd plotted on the assumption that all ice hydrometers are snowflakes with the radii of

100 micron; orange, red, and purple lines depict the empirical relationship lines referred to *Sassen and Liao* [1996], *Okamoto et al*. [2007], and *Heymsfield et al*. [2005], respectively.

Figure 7. THCS of effective ice radius in the bin model simulation from 1200 UTC on 22th to 1200UTC on 23th May 2001.

Figure 8. Same as Figure 2 (b) but for dBZe calculated with the application of the Ze-IWC relationships of (a) *Okamoto et al*. [2007] and (b) *Heymsfield et al*. [2005] to IWC calculated in the bin model simulation.

Figure 9. Same as Figure 2 (b), Figure 3 (b) and Figure 6 but for the test simulation with the mass equivalent radius decreased to the half in the calculation of the radar-signal simulator.

Figure 10. Same as Figure 2 (b), Figure 3 (b) and Figure 6 but for the test simulation with the forcible break-up of large-size snowflakes.

Figure 11. THCSs of the Doppler velocities (DV) (a) measured by the 95 GHz MIRAI Doppler radar, and calculated from the radar-signal simulator applied to the results of the (b) bin model simulations from 1200 UTC on 22th to 1200UTC on 23th May 2001.

Figure 12. CFADs of DV constructed from (a) the measurement by the 95 GHz

Doppler radar on MIRAI, and (b) the simulation by the bin model simulation.

Figure 13. Same as Figure 11 (a) and Figure 12 (b) but for the test simulation with the forcible break-up of large-size snowflakes.

Figure 14. Relationships between terminal falling velocities at 1000 hPa and melted-particle radii on bins.

Figure 15. Same as the couple of Figures 2 (b), 3 (b), 11 (b), and 12 (b) but for the result in the sensitivity simulation where the terminal velocities of all ice hydrometeors were equalized to those of droplets in all bins.

Figure 16. THCSs of ice water contents (IWC) simulated in (a) the original bin model simulation, (b) the sensitivity simulations using the setting in Figure 15, and (c) the bulk model simulation.

Figure 17. Same as Figure 6 but for the sensitivity simulation using the setting in Figure 15.

Figure 18. Latitude height cross-sections of the radar reflectivity factor in the case of nimbostratus on November 11, 2006 (a) measured by the CloudSat CPR and calculated using the Ze simulator applied to the results of (b) the original bin model simulation, (c) calculated with the application of the Ze-IWC relationships of *Okamoto et al*. [2007], calculated using the Ze simulator applied to the sensitivity

simulation results (d) where with the forcible break-up of large-size snowflakes, (e) where the terminal velocities of all ice hydrometeors were equalized to those of droplets in all bins, and (f) same as (c) but for using the attenuation in (e).

Figure 19. Same as Figure 18 but for the case of convective clouds on November 14, 2006.

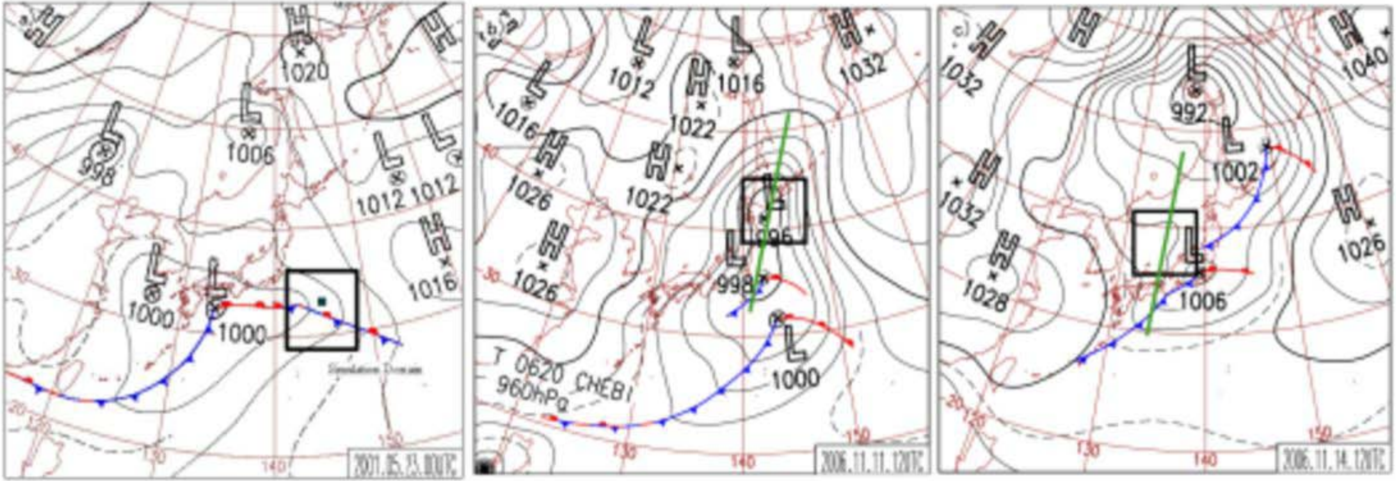
a
1020
1006
998
1012
1012
1000
1000
1016
Simulation Domain
2001.05.23.00UTC
b
1012
1016
1032
1016
1022
1026
1022
1026
996
998
1000
T 0620 CHEBI
960hPa
2006.11.11.12UTC
c
1032
992
1040
1002
1032
1026
1028
1006
2006.11.14.12UTC

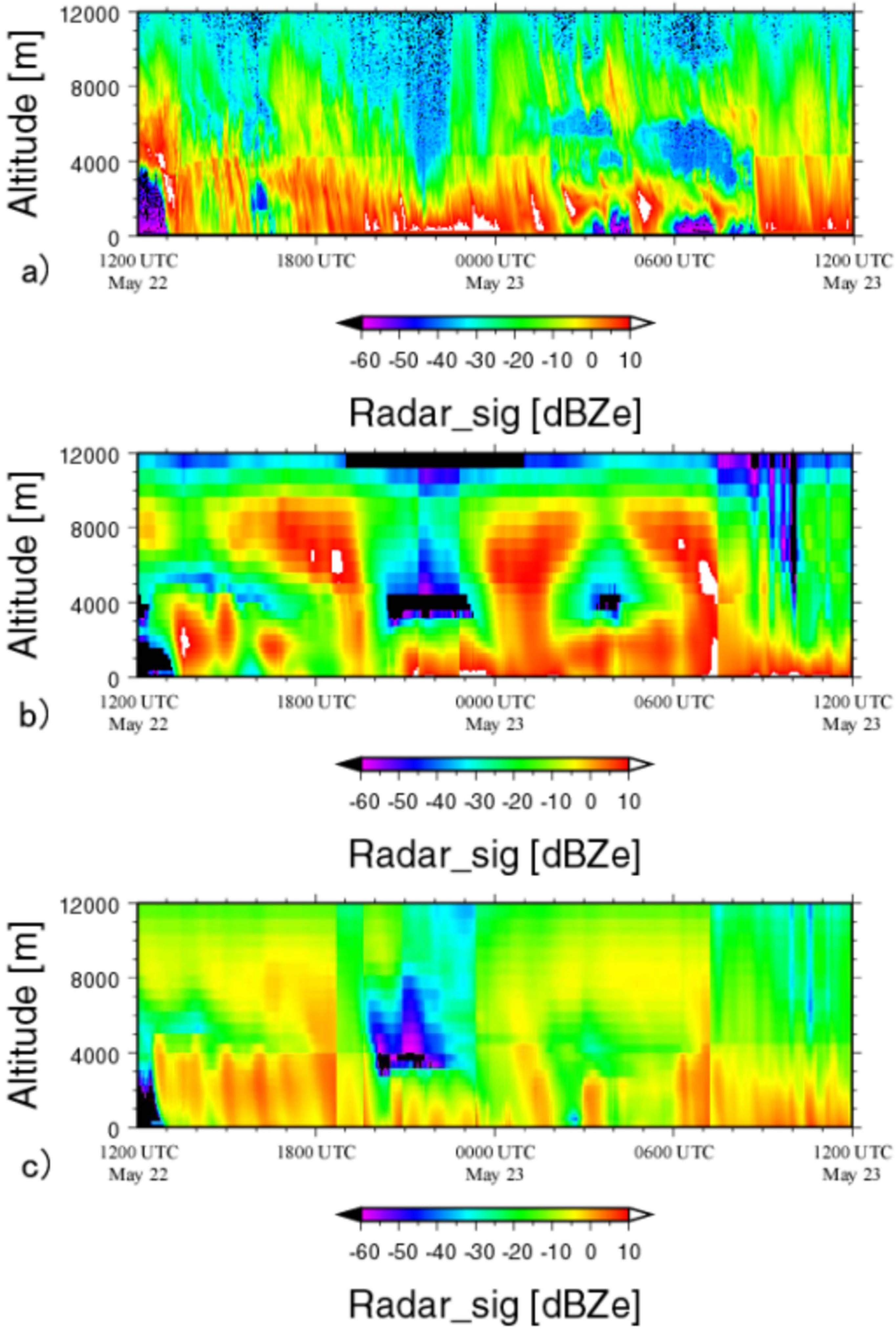
a)
b)
c)
Altitude [m]
0
4000
8000
12000
1200 UTC
May 22
1800 UTC
0000 UTC
May 23
0600 UTC
1200 UTC
May 23
-60 -50 -40 -30 -20 -10 0 10
Radar_sig [dBZe]

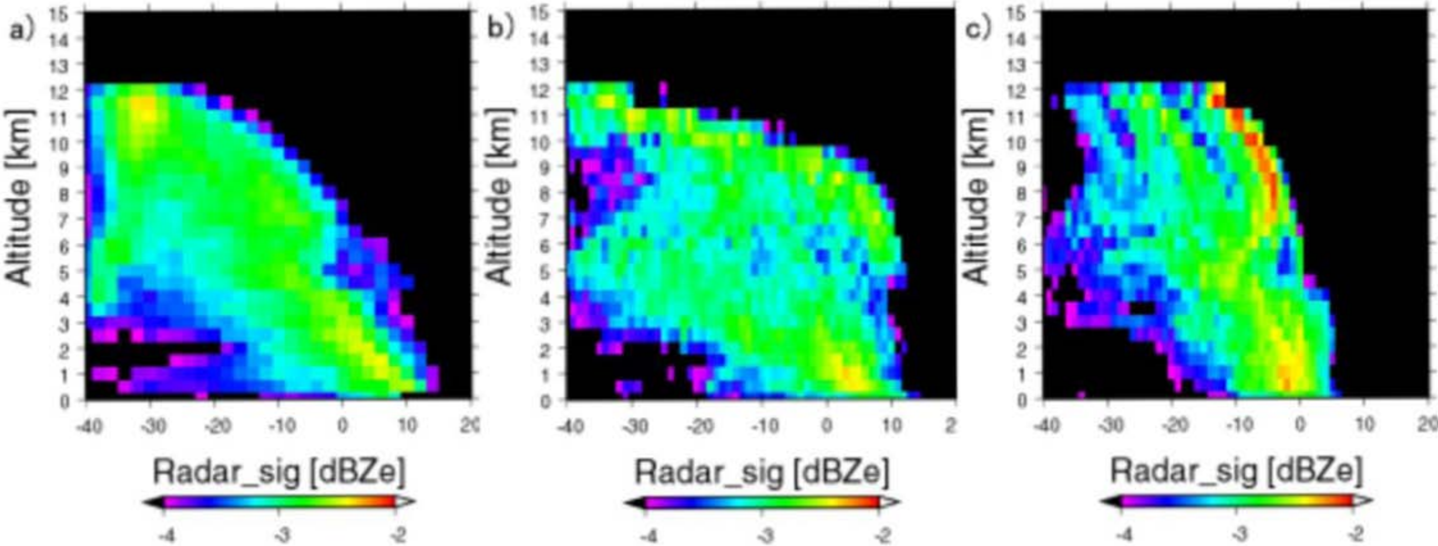
a)
b)
c)
Altitude [km]
0
1
2
3
4
5
6
7
8
9
10
11
12
13
14
15
-40
-30
-20
-10
0
10
20
Radar_sig [dBZe]
-4
-3
-2

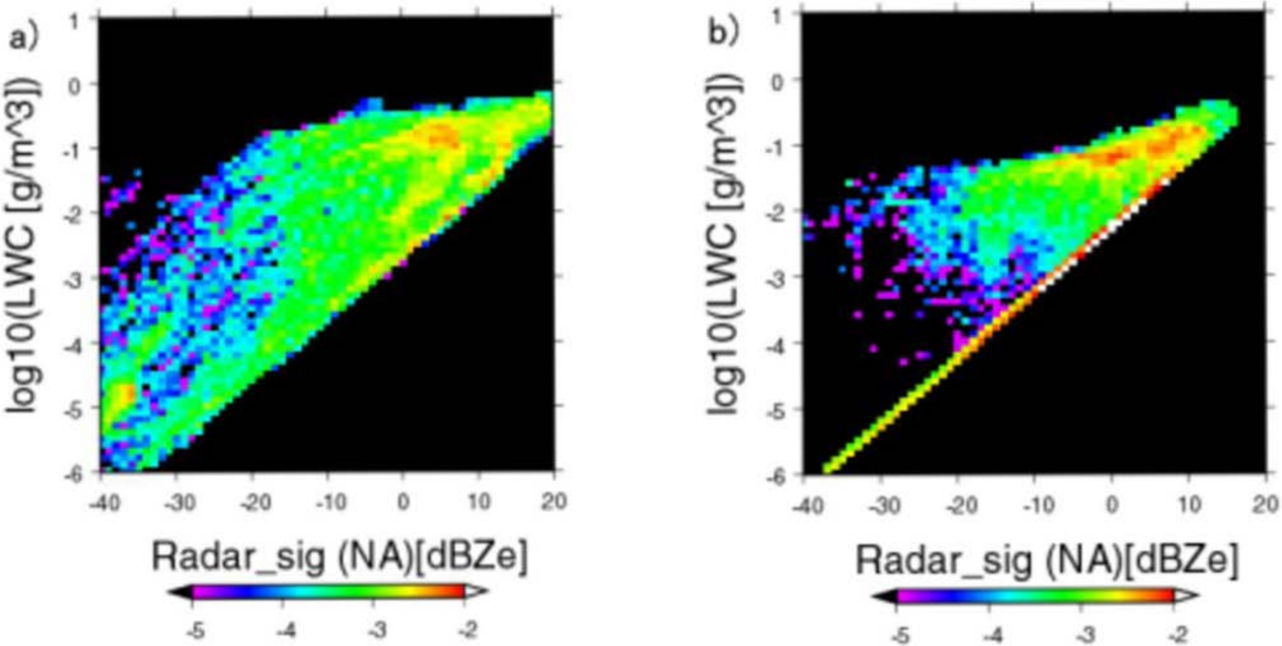
a)
log10(LWC [g/m^3])
1
0
-1
-2
-3
-4
-5
-6
-40
-30
-20
-10
0
10
20
Radar_sig (NA)[dBZe]
-5
-4
-3
-2
b)
log10(LWC [g/m^3])
1
0
-1
-2
-3
-4
-5
-6
-40
-30
-20
-10
0
10
20
Radar_sig (NA)[dBZe]
-5
-4
-3
-2

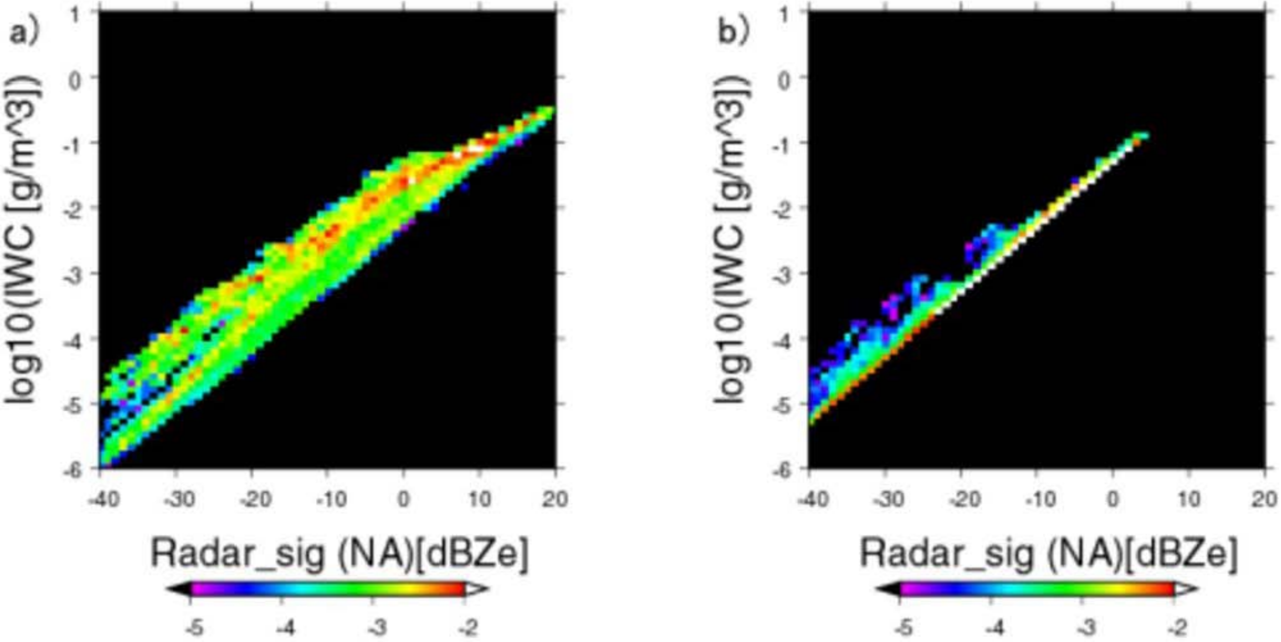
a)
b)
log10(IWC [g/m^3])
Radar_sig (NA)[dBZe]
1
0
-1
-2
-3
-4
-5
-6
-40
-30
-20
-10
0
10
20
-5
-4
-3
-2

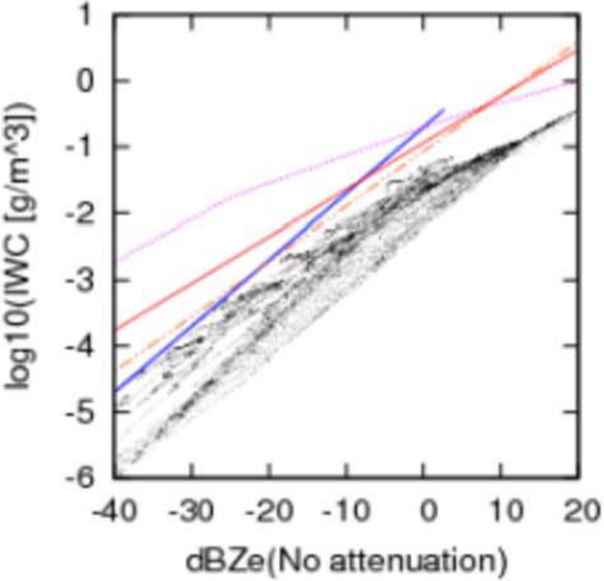
1
0
-1
-2
-3
-4
-5
-6
log10(IWC [g/m^3])
-40
-30
-20
-10
0
10
20
dBZe(No attenuation)

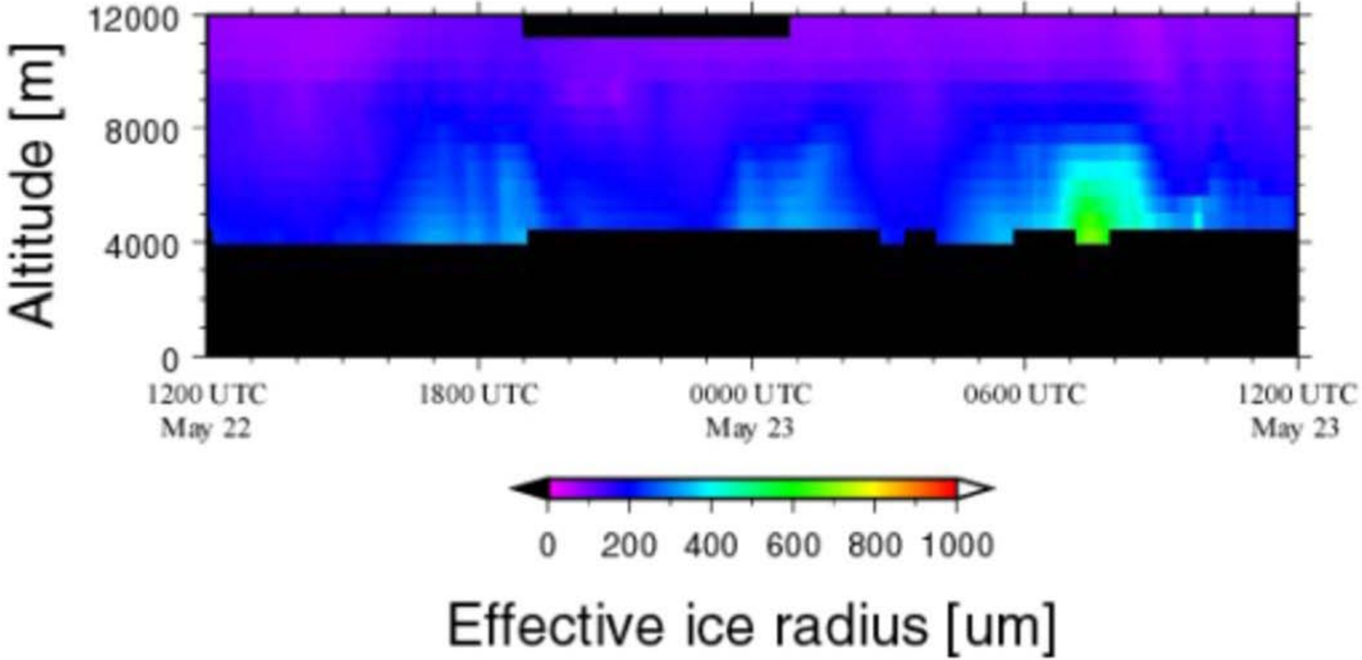
Altitude [m]
12000
8000
4000
0
1200 UTC May 22
1800 UTC
0000 UTC May 23
0600 UTC
1200 UTC May 23
0
200
400
600
800
1000
Effective ice radius [um]

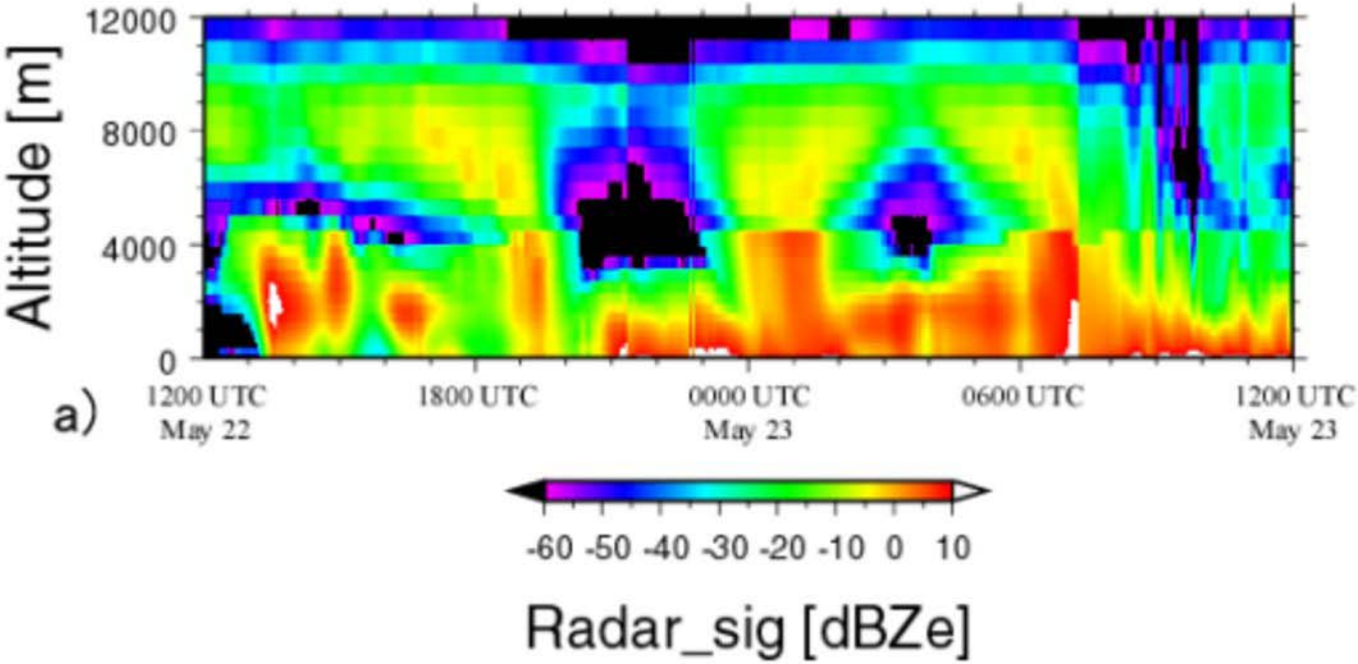
12000
8000
4000
0
Altitude [m]
a)
1200 UTC May 22
1800 UTC
0000 UTC May 23
0600 UTC
1200 UTC May 23
-60 -50 -40 -30 -20 -10 0 10
Radar_sig [dBZe]

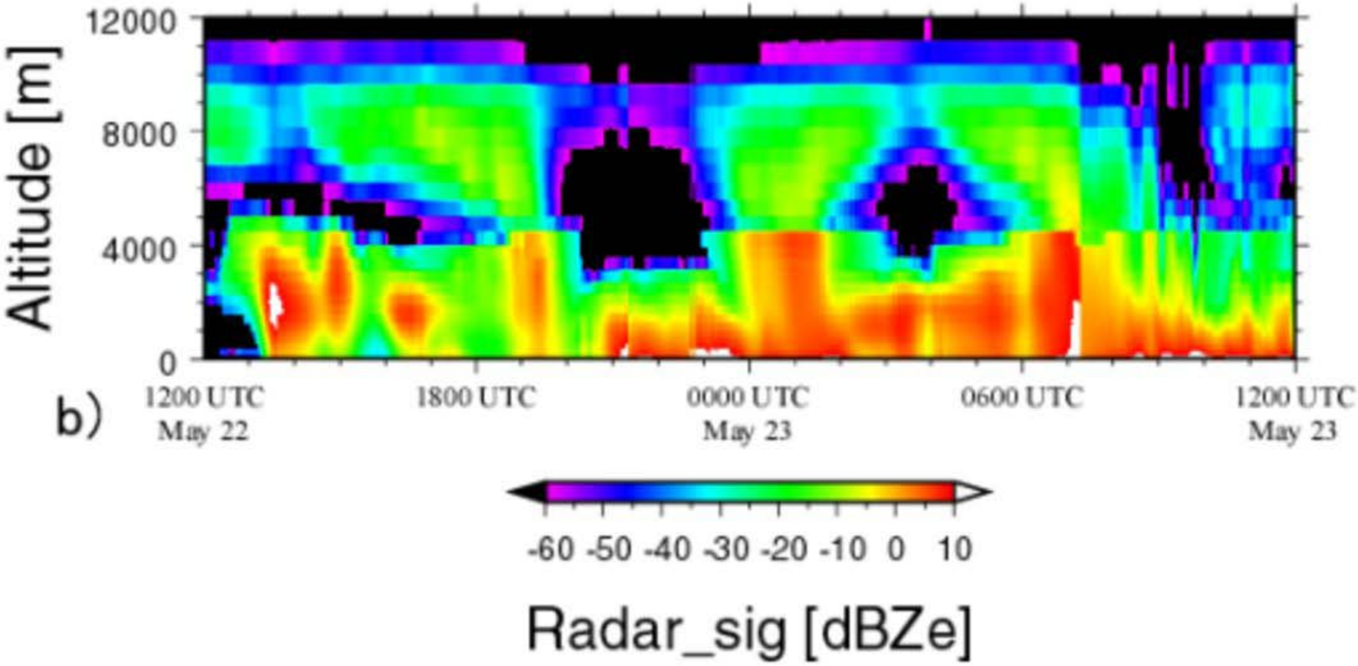
12000
8000
4000
0
Altitude [m]
b)
1200 UTC May 22
1800 UTC
0000 UTC May 23
0600 UTC
1200 UTC May 23
-60 -50 -40 -30 -20 -10 0 10
Radar_sig [dBZe]

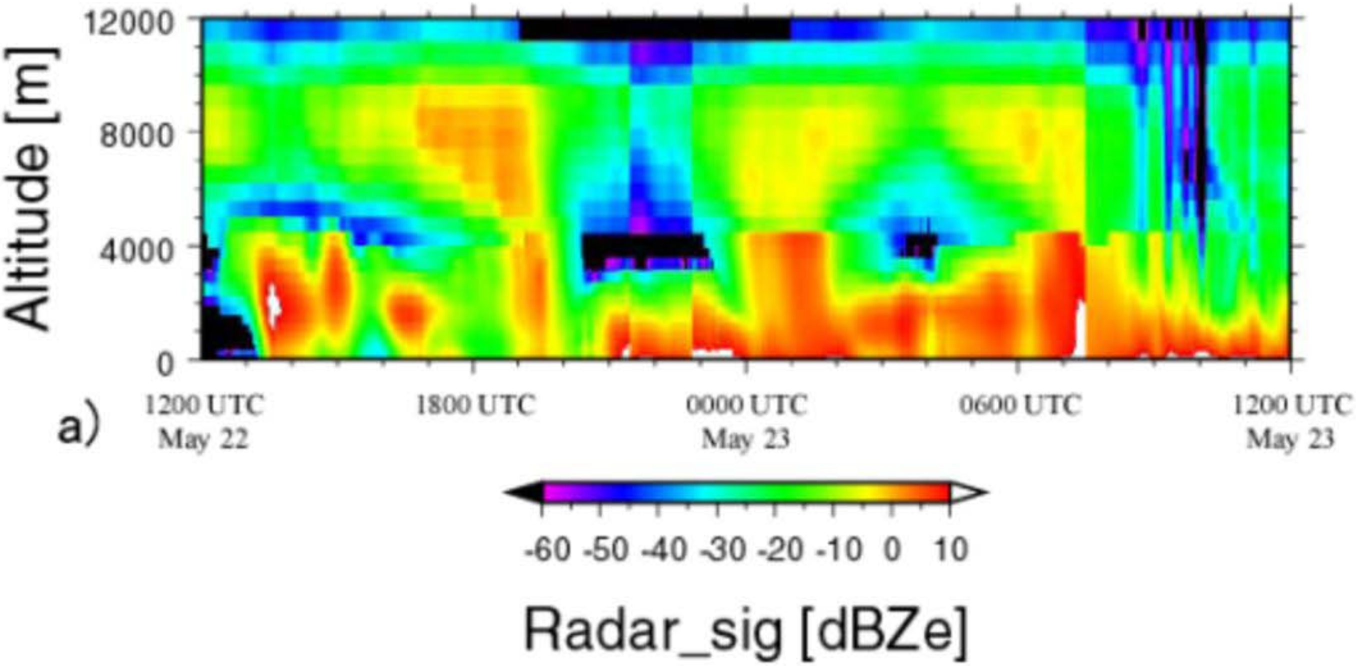
a)
Altitude [m]
12000
8000
4000
0
1200 UTC May 22
1800 UTC
0000 UTC May 23
0600 UTC
1200 UTC May 23
-60 -50 -40 -30 -20 -10 0 10
Radar_sig [dBZe]

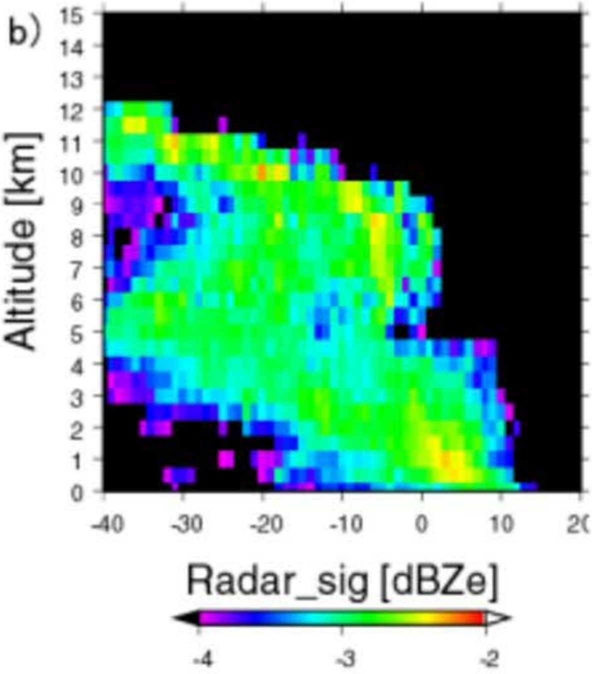
b)
Altitude [km]
15
14
13
12
11
10
9
8
7
6
5
4
3
2
1
0
-40
-30
-20
-10
0
10
20
Radar_sig [dBZe]
-4
-3
-2

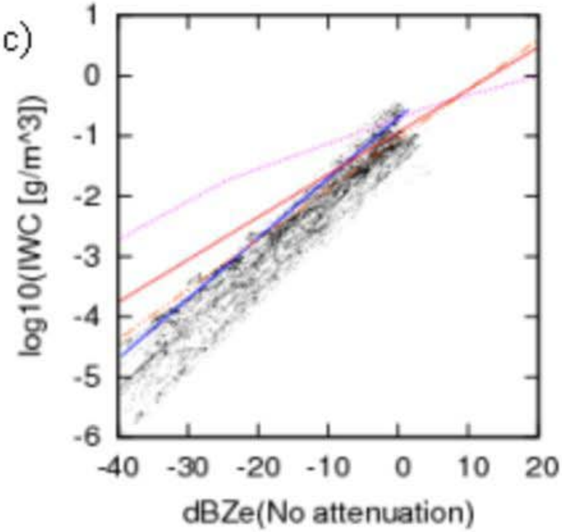
c)
log10(IWC [g/m^3])
1
0
-1
-2
-3
-4
-5
-6
-40
-30
-20
-10
0
10
20
dBZe(No attenuation)

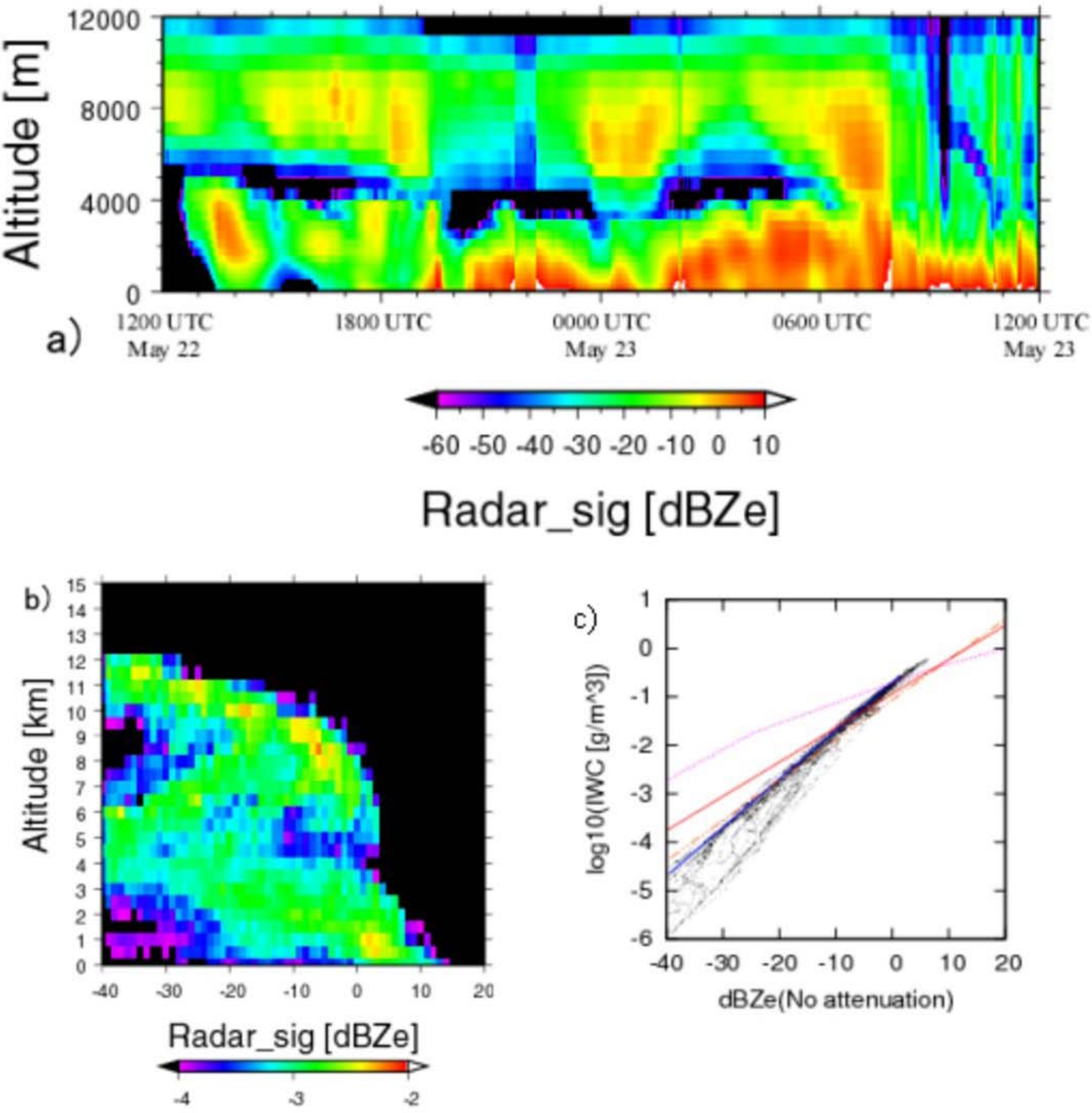
a)
Altitude [m]
12000
8000
4000
0
1200 UTC May 22
1800 UTC
0000 UTC May 23
0600 UTC
1200 UTC May 23
-60 -50 -40 -30 -20 -10 0 10
Radar_sig [dBZe]
b)
Altitude [km]
15 14 13 12 11 10 9 8 7 6 5 4 3 2 1 0
-40 -30 -20 -10 0 10 20
Radar_sig [dBZe]
-4 -3 -2
c)
log10(IWC [g/m^3])
1 0 -1 -2 -3 -4 -5 -6
-40 -30 -20 -10 0 10 20
dBZe(No attenuation)

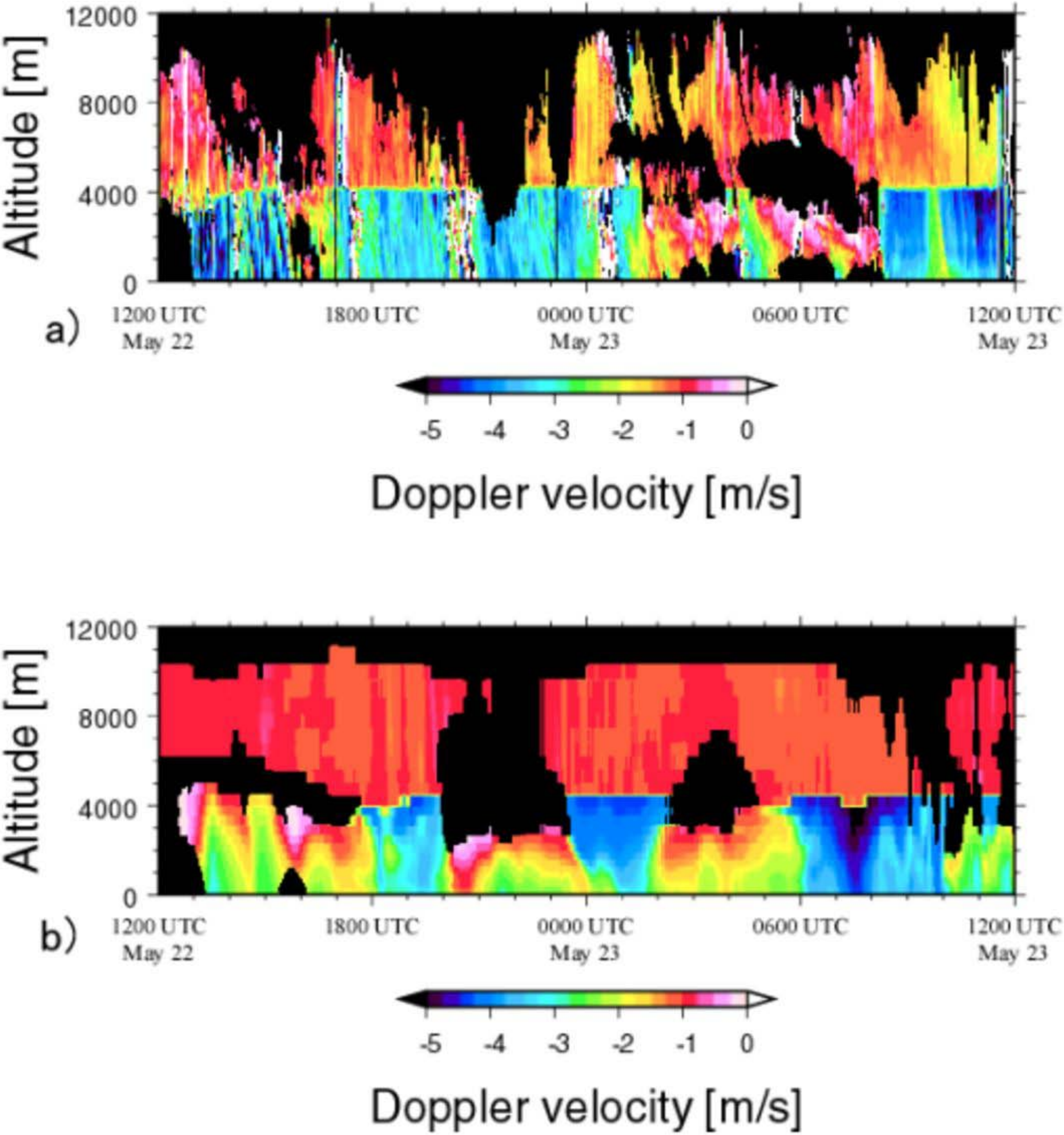
Altitude [m]
12000
8000
4000
0
a)
1200 UTC May 22
1800 UTC
0000 UTC May 23
0600 UTC
1200 UTC May 23
-5
-4
-3
-2
-1
0
Doppler velocity [m/s]
b)

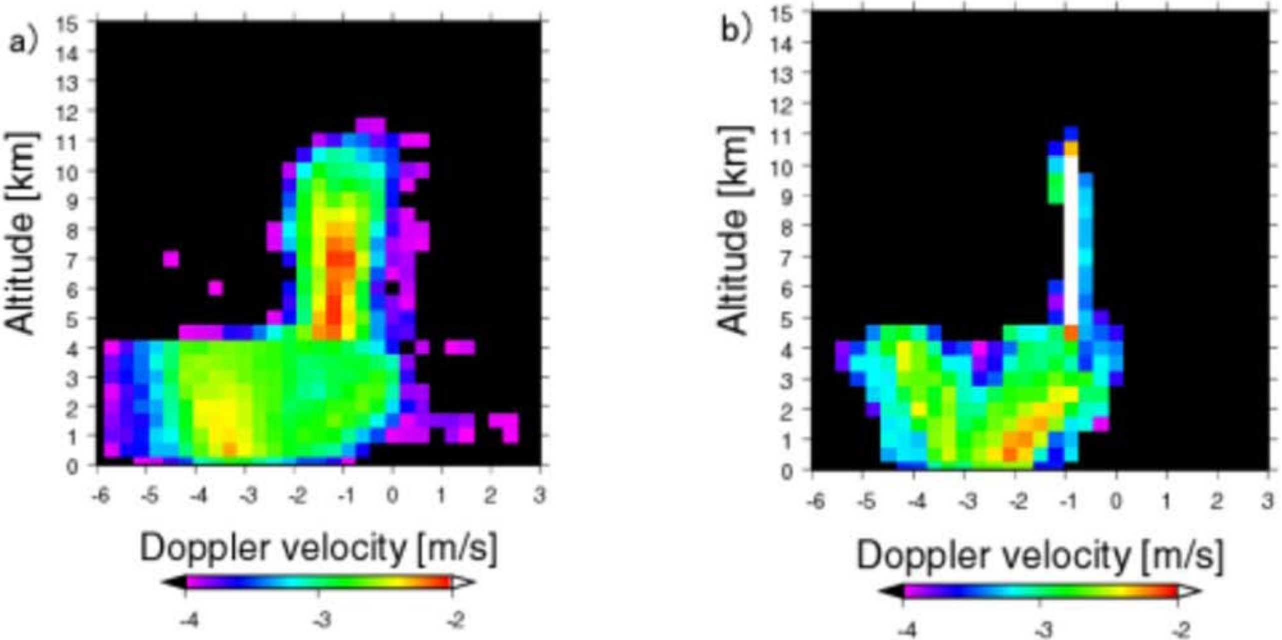
a)
Altitude [km]
0
1
2
3
4
5
6
7
8
9
10
11
12
13
14
15
-6
-5
-4
-3
-2
-1
0
1
2
3
Doppler velocity [m/s]
-4
-3
-2
b)
Altitude [km]
0
1
2
3
4
5
6
7
8
9
10
11
12
13
14
15
-6
-5
-4
-3
-2
-1
0
1
2
3
Doppler velocity [m/s]
-4
-3
-2

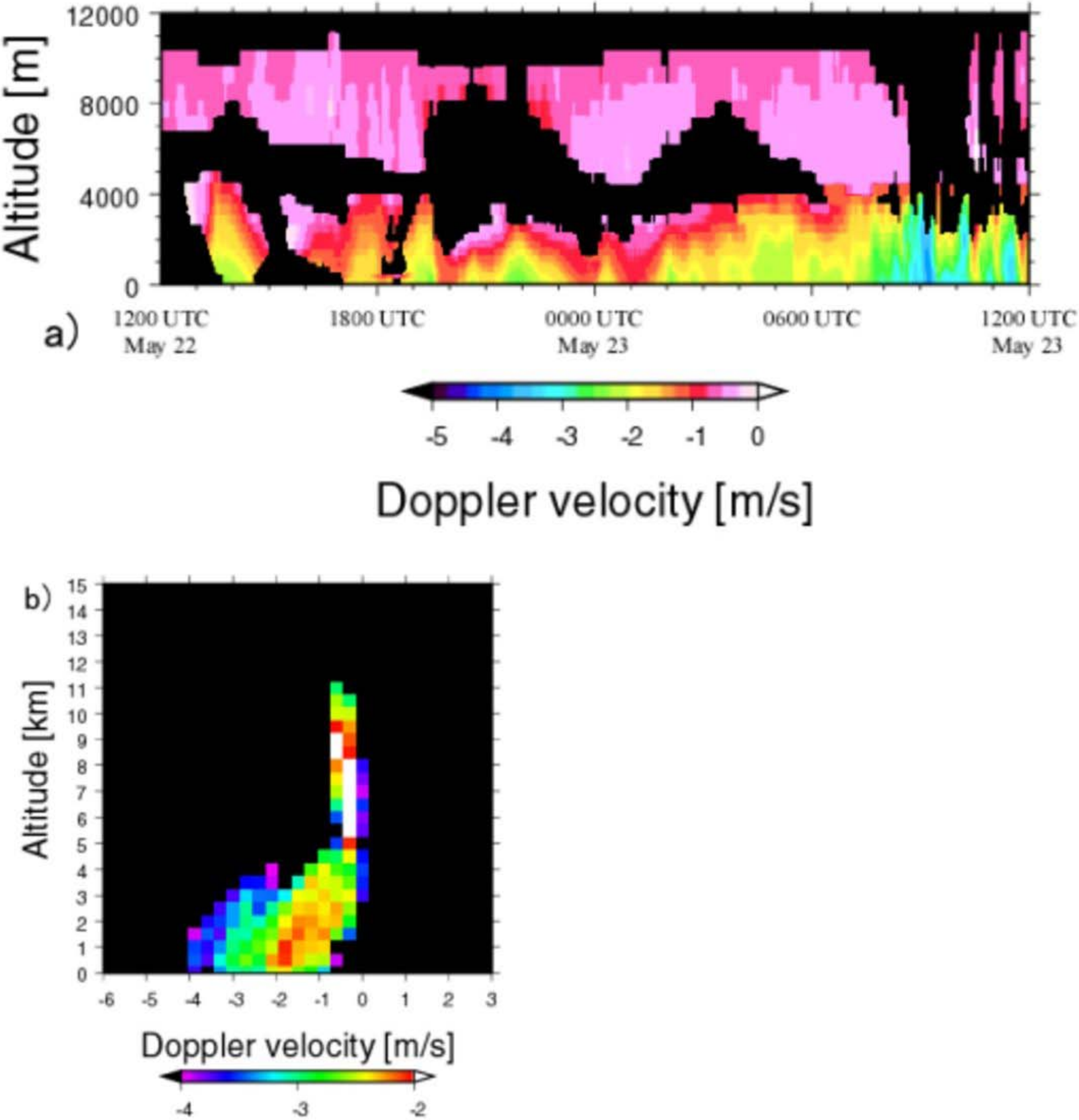
a)
Altitude [m]
12000
8000
4000
0
1200 UTC May 22
1800 UTC
0000 UTC May 23
0600 UTC
1200 UTC May 23
-5
-4
-3
-2
-1
0
Doppler velocity [m/s]
b)
Altitude [km]
15
14
13
12
11
10
9
8
7
6
5
4
3
2
1
0
-6
-5
-4
-3
-2
-1
0
1
2
3
Doppler velocity [m/s]
-4
-3
-2

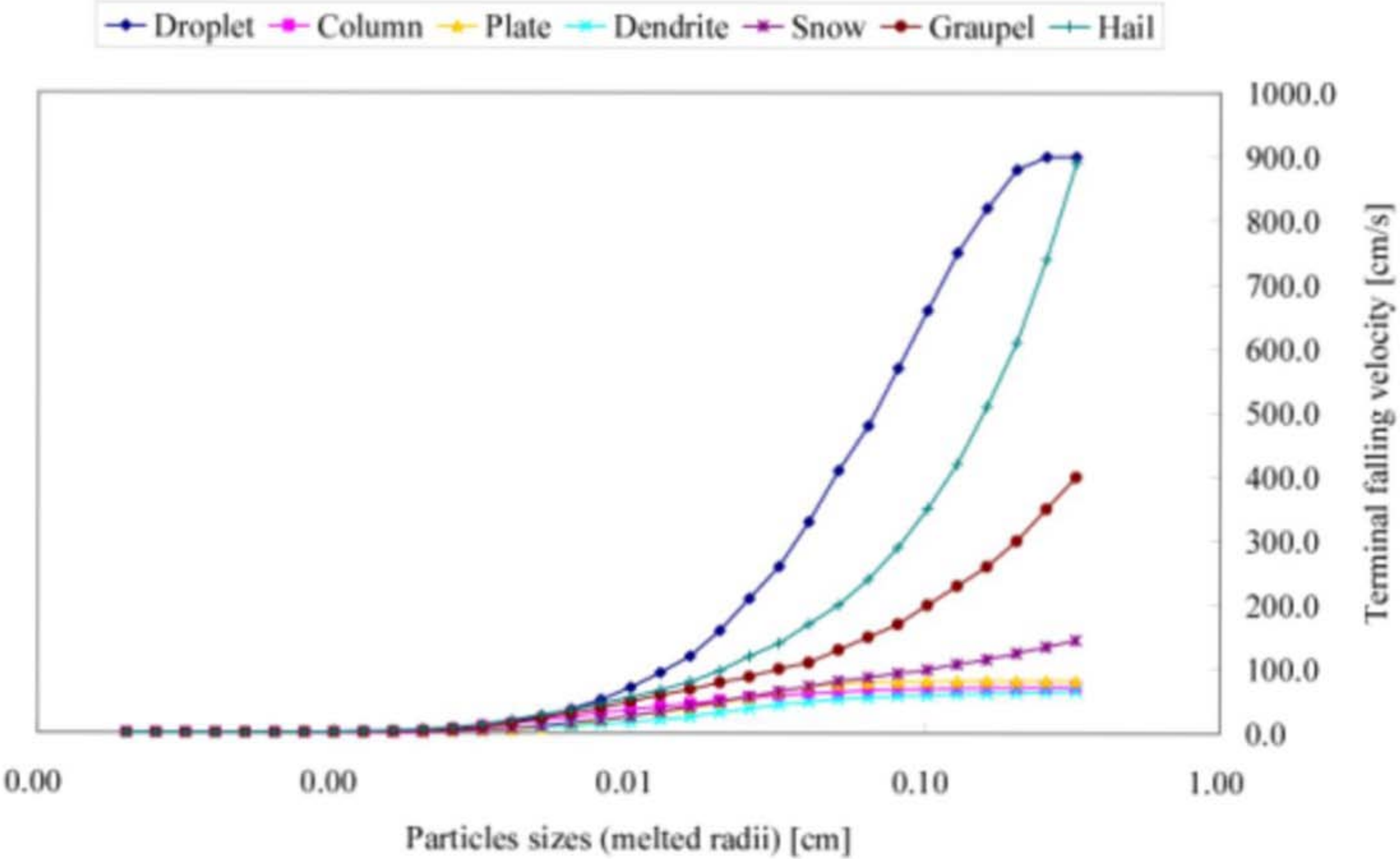
Droplet
Column
Plate
Dendrite
Snow
Graupel
Hail
1000.0
900.0
800.0
700.0
600.0
500.0
400.0
300.0
200.0
100.0
0.0
Terminal falling velocity [cm/s]
0.00
0.00
0.01
0.10
1.00
Particles sizes (melted radii) [cm]

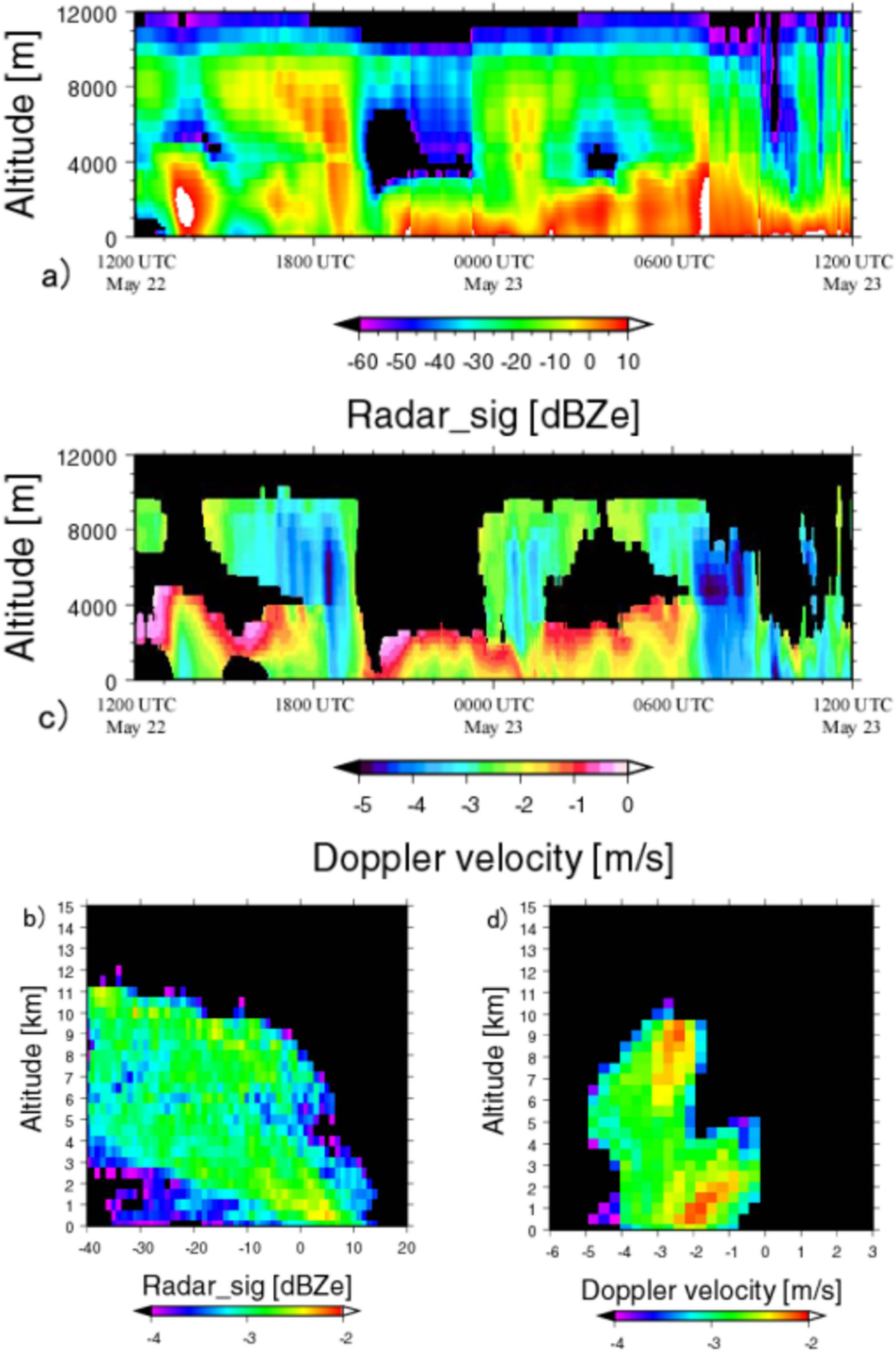
a)
Altitude [m]
12000
8000
4000
0
1200 UTC May 22
1800 UTC
0000 UTC May 23
0600 UTC
1200 UTC May 23
-60 -50 -40 -30 -20 -10 0 10
Radar_sig [dBZe]
c)
Altitude [m]
12000
8000
4000
0
1200 UTC May 22
1800 UTC
0000 UTC May 23
0600 UTC
1200 UTC May 23
-5 -4 -3 -2 -1 0
Doppler velocity [m/s]
b)
Altitude [km]
15 14 13 12 11 10 9 8 7 6 5 4 3 2 1 0
-40 -30 -20 -10 0 10 20
Radar_sig [dBZe]
-4 -3 -2
d)
Altitude [km]
15 14 13 12 11 10 9 8 7 6 5 4 3 2 1 0
-6 -5 -4 -3 -2 -1 0 1 2 3
Doppler velocity [m/s]
-4 -3 -2

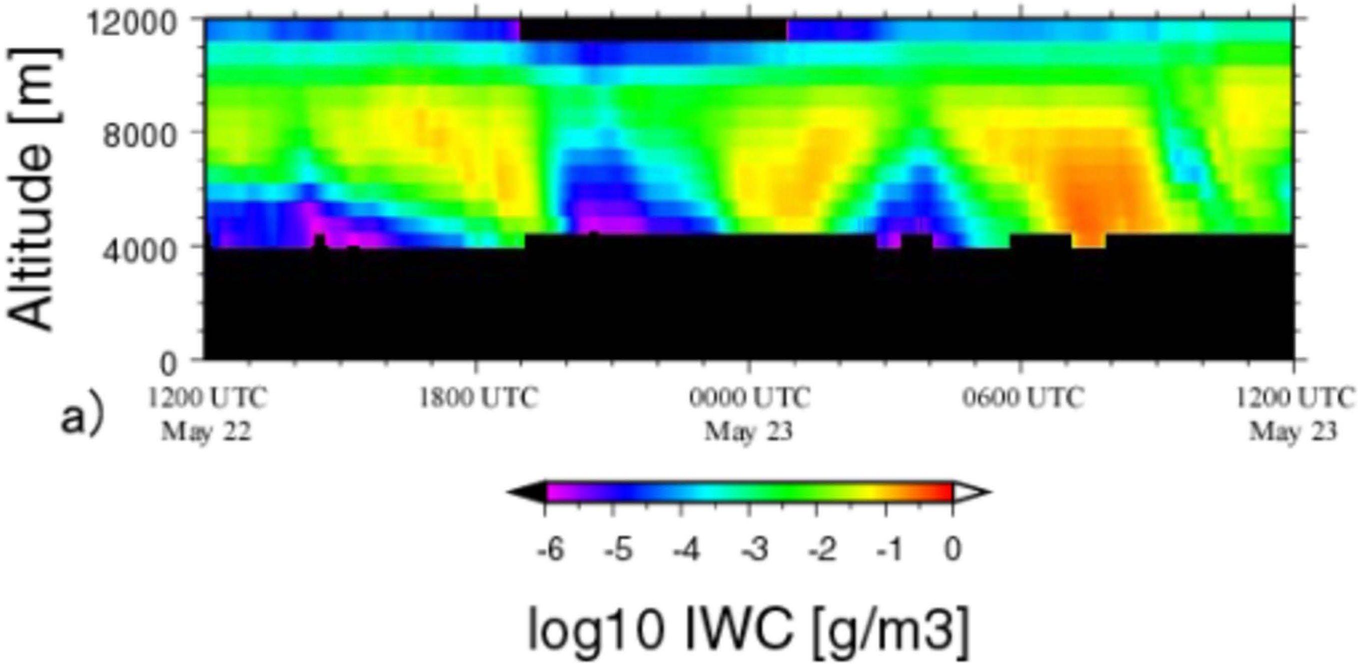
12000
8000
4000
0
Altitude [m]
1200 UTC May 22
1800 UTC
0000 UTC May 23
0600 UTC
1200 UTC May 23
-6
-5
-4
-3
-2
-1
0
log10 IWC [g/m3]

a)

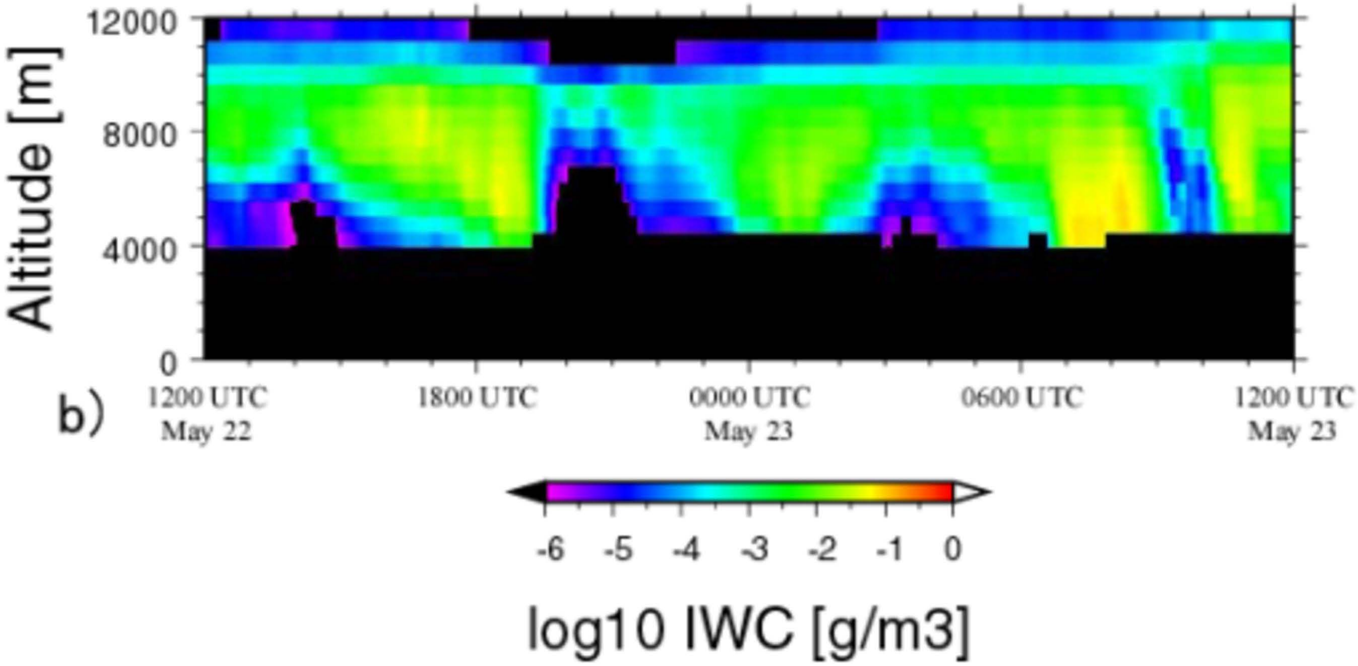
12000
8000
4000
0
Altitude [m]
1200 UTC May 22
1800 UTC
0000 UTC May 23
0600 UTC
1200 UTC May 23
-6
-5
-4
-3
-2
-1
0
log10 IWC [g/m3]

b)

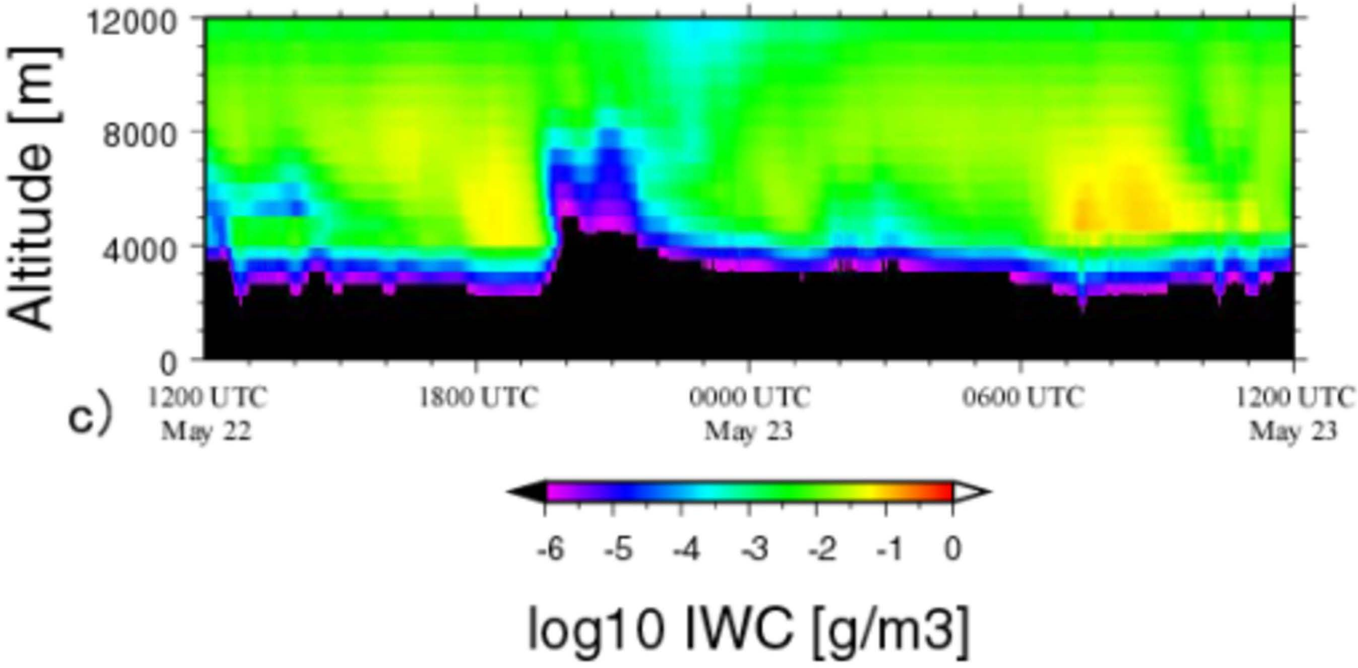
12000
8000
4000
0
Altitude [m]
1200 UTC May 22
1800 UTC
0000 UTC May 23
0600 UTC
1200 UTC May 23
-6
-5
-4
-3
-2
-1
0
log10 IWC [g/m3]

c)

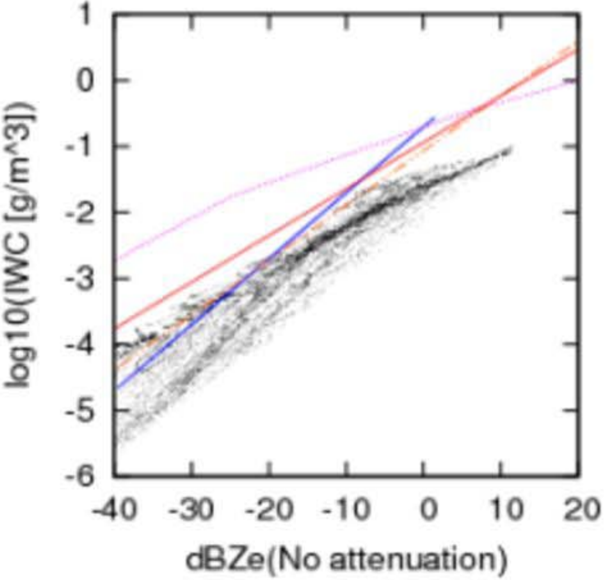
log10(IWC [g/m^3])
1
0
-1
-2
-3
-4
-5
-6
-40
-30
-20
-10
0
10
20
dBZe(No attenuation)

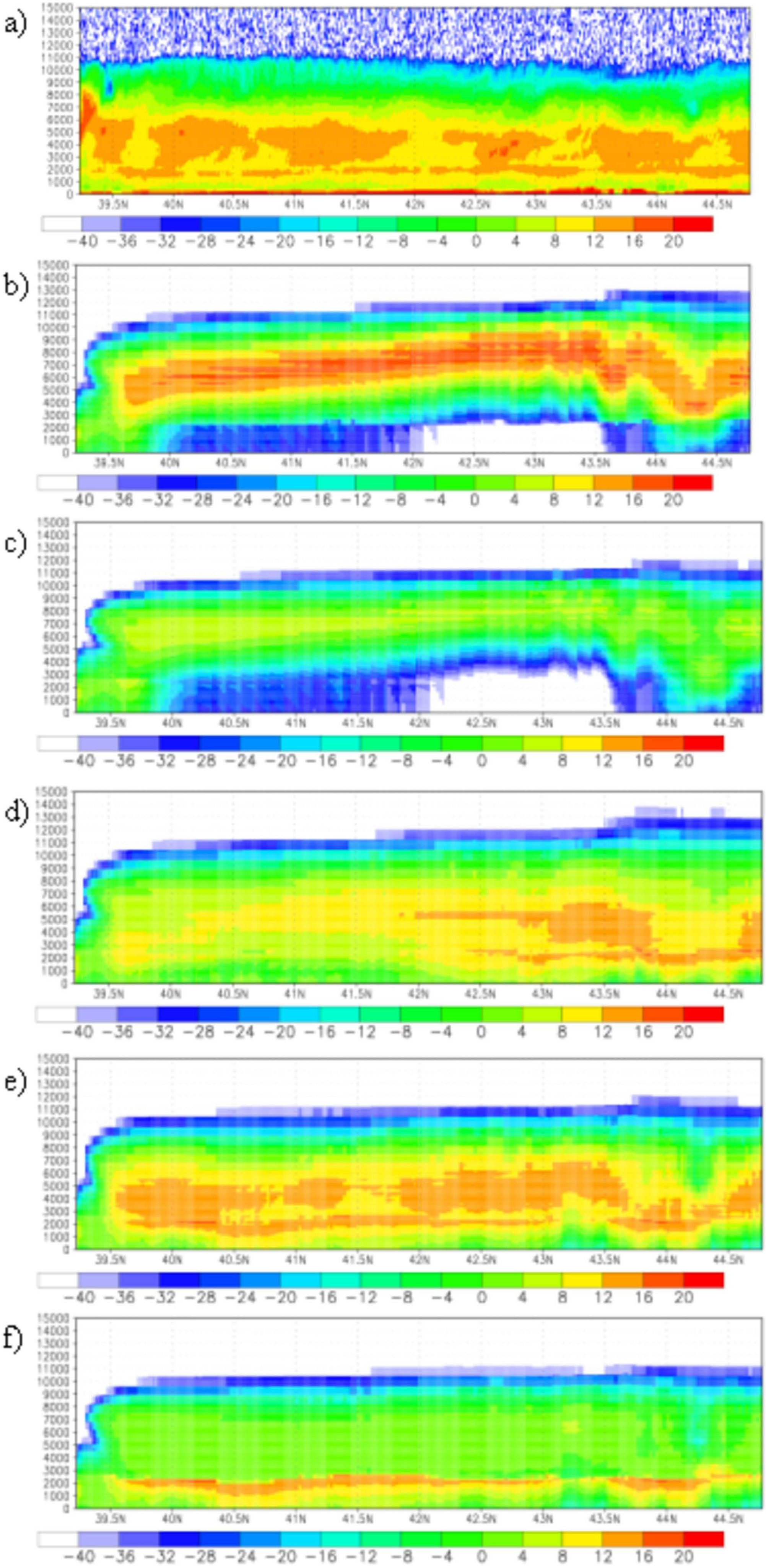
a)
b)
c)
d)
e)
f)
15000
14000
13000
12000
11000
10000
9000
8000
7000
6000
5000
4000
3000
2000
1000
0
39.5N
40N
40.5N
41N
41.5N
42N
42.5N
43N
43.5N
44N
44.5N
-40
-36
-32
-28
-24
-20
-16
-12
-8
-4
0
4
8
12
16
20

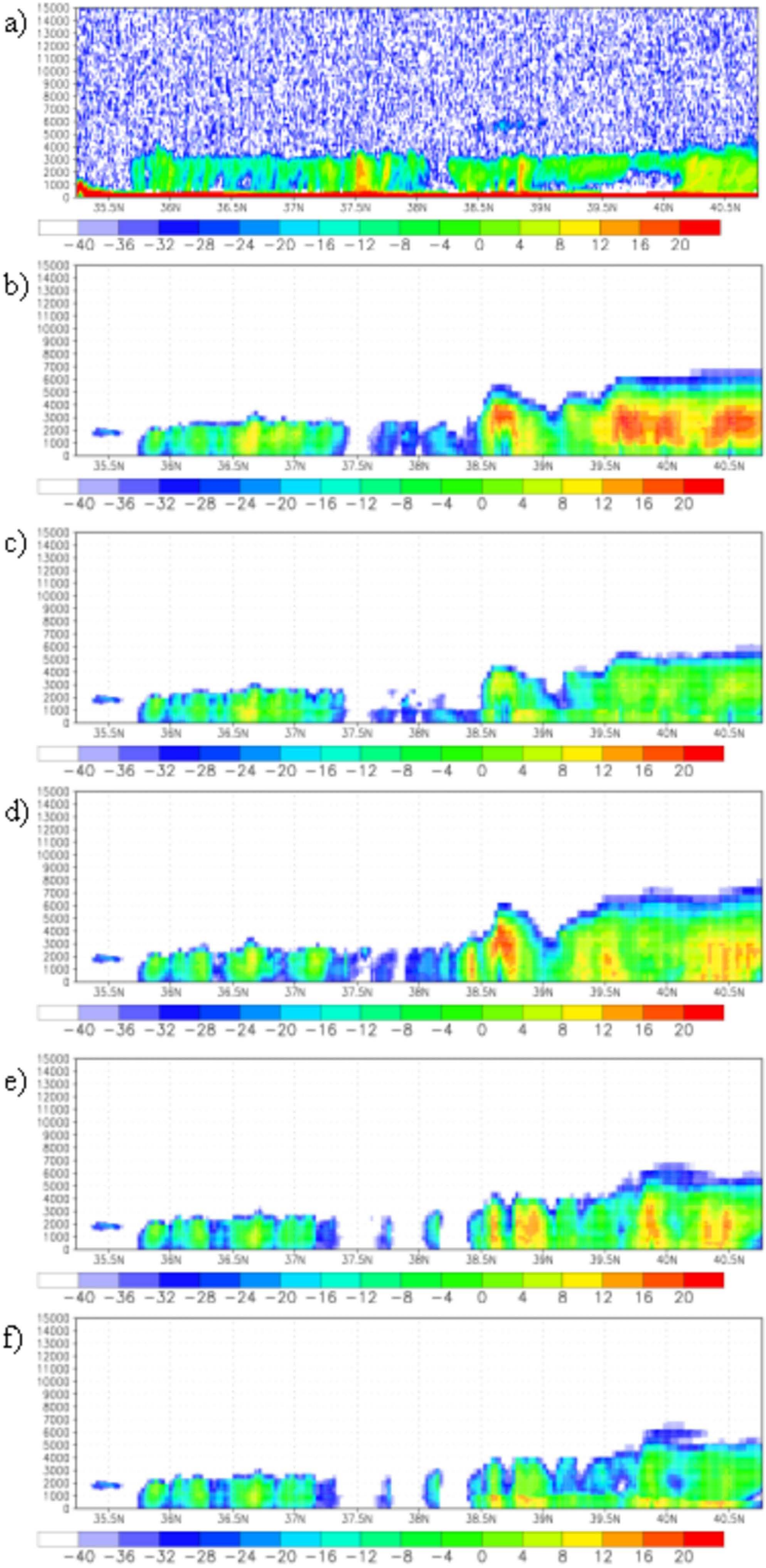
a)
b)
c)
d)
e)
f)
15000
14000
13000
12000
11000
10000
9000
8000
7000
6000
5000
4000
3000
2000
1000
0
35.5N
36N
36.5N
37N
37.5N
38N
38.5N
39N
39.5N
40N
40.5N
-40
-36
-32
-28
-24
-20
-16
-12
-8
-4
0
4
8
12
16
20

Evaluation of cloud microphysics simulated using a meso-scale model coupled with a spectral bin microphysical scheme through comparison with observation data by ship-borne Doppler and space-borne W-band radars

T. Iguchi, T. Nakajima, A. P. Khain, K. Saito, T. Takemura, H. Okamoto,
T. Nishizawa, and W.-K. Tao

Submitted to J. Geophy. Res.

Popular Summary

Equivalent radar reflectivity factors (Ze) measured by W-band radars are directly compared with the corresponding values calculated from a three-dimensional non-hydrostatic meso-scale model coupled with a spectral-bin-microphysical (SBM) scheme for cloud. Three case studies are the objects of this research: one targets a part of ship-borne observation using 95 GHz Doppler radar over the Pacific Ocean near Japan in May 2001; other two are aimed at two short segments of space-borne observation by the cloud profiling radar on CloudSat in November 2006. The numerical weather prediction (NWP) simulations reproduce general features of vertical structures of Ze and Doppler velocity. A main problem in the reproducibility is an overestimation of Ze in ice cloud layers. A frequency analysis shows a strong correlation between ice water contents (IWC) and Ze in the simulation; this characteristic is similar to those shown in prior on-site studies. From comparing with the empirical correlations by the prior studies, the simulated Ze is overestimated than the corresponding values in the studies at the same IWC. Whereas the comparison of Doppler velocities suggests that large-size snowflakes are necessary for producing large velocities under the freezing level and hence rules out the possibility that an overestimation of snow size causes the overestimation of Ze. Based on the results of several sensitivity tests, we conclude that the source of the overestimation is a bias in the microphysical calculation of Ze or an overestimation of IWC. To identify the source of the problems needs further validation research with other follow-up observations.